IDEA League

MASTER OF SCIENCE IN APPLIED GEOPHYSICS

RESEARCH THESIS

Near-Surface Characterization of Mars InSight Data by Polarization Analysis

651-1062-00L, Master's Thesis

17-931-189, Xenia Sarah Meier-Ruge

August 5, 2022

Near-Surface Characterization of Mars InSight Data by Polarization Analysis

651-1062-00L, Master's Thesis

MASTER OF SCIENCE THESIS

for the degree of Master of Science in Applied Geophysics

by

17-931-189, Xenia Sarah Meier-Ruge

August 5, 2022

IDEA LEAGUE
JOINT MASTER'S IN APPLIED GEOPHYSICS

Delft University of Technology, The Netherlands
ETH Zürich, Switzerland
RWTH Aachen, Germany

Dated: *August 5, 2022*

Supervisor(s):

_____
Dr. Pascal Edme, ETHZ, Institute of Geophysics

_____
Dr. David Sollberger, ETHZ, Institute of Geophysics

_____
Ph.D. at D-ERDW, Nienke Brinkman, ETHZ, Institute of Geophysics

Committee Members:

_____
Dr. Pascal Edme, ETHZ, Institute of Geophysics

_____
Prof. E. C. Slob, TU Delft, Faculty of Civil Engineering and Geosciences

_____
Dr. David Sollberger, ETHZ, Institute of Geophysics

ETH

Eidgenössische Technische Hochschule Zürich
Swiss Federal Institute of Technology Zurich

Eigenständigkeitserklärung

Die unterzeichnete Eigenständigkeitserklärung ist Bestandteil jeder während des Studiums verfassten Semester-, Bachelor- und Master-Arbeit oder anderen Abschlussarbeit (auch der jeweils elektronischen Version).

Die Dozentinnen und Dozenten können auch für andere bei ihnen verfasste schriftliche Arbeiten eine Eigenständigkeitserklärung verlangen.

Ich bestätige, die vorliegende Arbeit selbständig und in eigenen Worten verfasst zu haben. Davon ausgenommen sind sprachliche und inhaltliche Korrekturvorschläge durch die Betreuer und Betreuerinnen der Arbeit.

Titel der Arbeit (in Druckschrift):

Near-Surface Characterization of Mars InSight Data by Polarization Analysis

Verfasst von (in Druckschrift):
Bei Gruppenarbeiten sind die Namen aller Verfasserinnen und Verfasser erforderlich.

Name(n):	**Vorname(n):**
Meier-Ruge	Xenia Sarah

Ich bestätige mit meiner Unterschrift:
- Ich habe keine im Merkblatt „Zitier-Knigge" beschriebene Form des Plagiats begangen.
- Ich habe alle Methoden, Daten und Arbeitsabläufe wahrheitsgetreu dokumentiert.
- Ich habe keine Daten manipuliert.
- Ich habe alle Personen erwähnt, welche die Arbeit wesentlich unterstützt haben.

Ich nehme zur Kenntnis, dass die Arbeit mit elektronischen Hilfsmitteln auf Plagiate überprüft werden kann.

Ort, Datum

05.08.2022 , Zurich

Unterschrift(en)

Bei Gruppenarbeiten sind die Namen aller Verfasserinnen und Verfasser erforderlich. Durch die Unterschriften bürgen sie gemeinsam für den gesamten Inhalt dieser schriftlichen Arbeit.

Abstract

On the 25th of November 2018, NASA's InSight Mars-lander landed at Elysium Planitia on Mars (NASA, 2022a). The lander includes the SEIS instrument, which measures the seismic signals on the planet (NASA, 2022b). Because seismic waves are altered by the medium they travel through from the source to the receiver, they contain information on the interior structure of the planet. This information about the structure of Mars can be extracted by applying different data processing and evaluation techniques.

One of the proposed methods is the polarization analysis of the first-arriving P-wave, which is expected to contain information about the near-surface S-wave velocity structure. The technique uses the polarization of an incoming P-wave in horizontal and radial direction to estimate the apparent P-wave incidence angle (Knapmeyer-Endrun et al., 2018). The measured P-wave incidence angle can further be used to estimate a frequency-dependent S-wave velocity from the first break, given that the ray parameter is known. An inversion of such frequency-dependent S-wave velocity curves can then potentially lead to velocity-depth profiles of the near-surface zone.

A first pre-testing of the polarization analysis on a synthetic model should help to understand the process of frequency-dependent S-wave velocity extraction and to work out the limitations of the method. The synthetic data testing showed, that there are a range of important parameters, which influence the velocity estimation. It is highly frequency-dependent and later arrivals, as well as noise, can affect the accuracy. One of the indicators that can be used to evaluate whether or not the extracted S-wave velocities can be trusted is the ellipticity of the polarized wave, which should not be above a threshold of 0.2. The time delay between the P- and the mode-converted PS-arrival (defined as Δt_{app}) could be used to define the areas where the estimated velocities change from their expected value. It was found, that Δt_{app} has to be greater than 1.4×1e-4 - 2×1e-4 s, that a velocity estimation of the first layer is possible. This is valid for frequencies between 0.08 Hz up to 6 Hz. The second layer velocity could only be calculated for frequencies lower than 0.6 - 2 Hz for the tested models. Furthermore, a proper velocity extraction is not possible for certain Δt_{app} and frequency combinations because the angle estimation in this area can not be calculated properly, so far. However, synthetic tests showed that the velocities of a two-layer model could be extracted for specific first layer thicknesses in a given frequency-range and a following basic inversion enabled the

extraction of the interface depth between these layers.

The application of the polarization analysis to two Martian events allowed a frequency-dependent V_s-velocity extraction for the event S1222a, as 2451 m/s and 2665 m/s for the frequencies of 0.21 Hz and 1.43 Hz respectively. These values could be further used to compare with velocity extractions from other methods. For the second event S0235b, the ellipticity of the first break was above the 0.2 threshold and did therefore not lead to trustworthy outcomes. The polarization analysis applied to real data showed, that a velocity calculation is challenging but possible under certain conditions. Many parameters like the source and its frequency content should be known to actually invert the data, which is why a further analysis with receiver functions is recommended. For further processing, an extended synthetic data testing for other parameters should be performed.

Acknowledgements

Table of Contents

List of Figures

List of Tables

Acronyms

DUT Delft University of Technology

ETHZ Swiss Federal Institute of Technology, Zurich

RWTH Aachen University

SEIS Seismic Experiment for Interior Structure - InSight's seismometer package

HP^3 Heat Flow and Physical Properties Package - Temperature Measurement

SP Short period seismometer, three-component seismometer

VBB Very broadband seismometer, three-component seismometer

RISE Rotation and Interior Structure Experiment - Radio Science Instrument on InSight

RMS Root Mean Squares

CWT 1-D wavelet transform with MATLAB$^{®}$

MQS Marsquake service

Chapter 1

Introduction

1-0-1 The InSight Project

New techniques and measurement methods allow us to measure seismic waves on planets like Mars. By analysing seismic waves, subsurface information can be extracted and be used to learn more about the formation of the planet and other rocky celestial bodies (ETHZ, 2021; NASA, 2022d). To measure the Martian tectonic activity, meteorite impacts and the planet's interior structure and composition (NASA, 2022c), NASA's InSight mission sent a lander to Mars, which landed on the 26th of November 2018 at Elysium Planitia. The three main instruments on board, SEIS, HP^3 and RISE, measure seismic waves, the heat flow, and the rotation of the planet, respectively (ETHZ, 2021). Since the start of the recording, multiple seismic events were recorded (marsquakes and impacts) and further used in various studies to determine the layering and internal structure of the planet. In a case study in preparation for InSight Knapmeyer-Endrun et al. (2018) proofed that the angle of subsurface particle motion of an incident P-wave, together with the corresponding horizontal slowness can be used to calculate the S-wave velocity. Further could Stähler et al. (2021) and Khan et al. (2021) divide the Martian structure into a primordial crust, a mantle and a liquid-metal core, which gives a first seismic based constraint structure definition. The really shallow subsurface structure at the landing site, up to 200 m depth, was characterized by Hobiger et al. (2021) by using ambient seismic vibrations. The part which is not well studied yet, are the layers in between the surface down to a few kilometers. To investigate this less constrained part, a method based on polarization analysis of seismic waves was tested in this thesis to explore whether it could be used to extract valuable subsurface information in that depth range.

1-0-2 Polarization Analysis

InSight's SEIS package consists of two three-component seismometers: a short period seismometer (called SP) and a very broadband seismometer (called VBB), each measuring ground motion due to incoming seismic waves, caused by Martian tectonic activity or meteorite impacts. The two seismometers have different sensitivities targeted to different frequency bands.

Both sensors measure the particle motion in three orthogonal components enabling the application of polarization analysis techniques. The polarization of the waves, a 3D particle motion as a function of time, can be used to estimate the apparent incidence angle of P-waves at the free surface that we want to use in this thesis to calculate frequency-dependent near-surface S-wave velocities. The S-wave velocity is an important parameter to interpret the subsurface composition with the goal to learn more about the structure of the planet. This thesis is done as a study to evaluate, to which extent the described polarization analysis technique can be used to extract subsurface information from Martian data and where the limitations of that method are. For this purpose, several tests were performed using both synthetics and actual data from Mars.

The two seismic events used in this thesis for the polarization analysis were measured on May 4th, 2022 and July 26th, 2019. With the exception of the event that occurred on the 4th of May, 2022, with an estimated magnitude of 4.7, all marsquake seismograms are characterized by a relatively low signal-to-noise ratio due to their low magnitudes. Figure 1-1 shows the recorded event from the 4th of May, 2022. The black and red line show the particle motion in Z- and R-direction. The blue dot shows the onset of the P-wave arrival. The data is already pre-processed to remove noise and glitches (Scholz et al., 2020). The example of this event illustrates the difficulty to apply polarization analysis to real data, because real Martian data is quite complex and it is strongly influenced by reverberations, scattering and other wave types, even though this is high-quality data. By applying the polarization analysis to real data, it is important to know in advance, which parameters influence the velocities that are extracted from the P-wave apparent incidence angles and to estimate the accuracy of the calculation when applying it to a real dataset. To work out these parameters, the method was briefly tested with synthetic data.

1-0-3 Importance of a Synthetic Data Testing

Additionally to the complexity of Martian data, the number of events that are available are limited and the data are recorded only by a single-station seismometer (i.e., the data correspond a point measurement). Also, so far only little information on the interior velocity structure of Mars is available in the depth range of interest for this project and strong trade-offs exist between the parametrization of subsurface velocity models and the location of the source. To minimize the uncertainties, we conducted a range of extensive tests using synthetic data obtained from a reflectivity code in a realistic near-surface model in order to evaluate the robustness of the polarization analysis scheme for S-wave velocity extraction. Since all input parameters are known for the given model, it can be used to define the limitations by cross-checking with the input. A following grid search and inversion was tested, to check if the relevant information can be extracted. This would then allow further application to a real dataset. For that purpose, this thesis focuses strongly on the synthetic data testing, with the aim to define limitations and to work out the important parameters which can be used as a foundation for further data processing and real data applications.
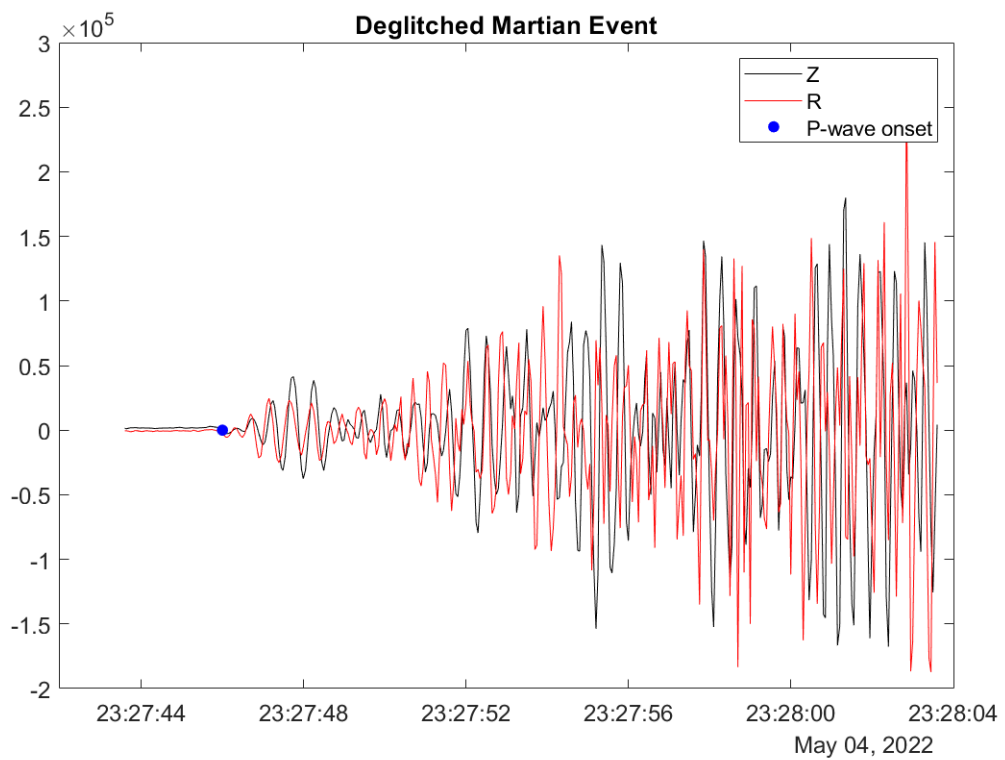
Figure 1-1: Deglitched Martian event, recorded on the 4th of May, 2022. Black line: Particle motion in Z-direction. Red line: Particle motion in R-direction. Blue dot: Marks the onset of the P-wave arrival. The figure shows the first 20 seconds of a recorded event on Mars. The data is already pre-processed and deglitched but still contains a lot of undesired reverberations (InSight Mars Data Service, 2022).

Chapter 2

Method

To extract velocity information of the subsurface and to invert for the interface depth, the polarization analysis was applied to a synthetic dataset generated by a reflectivity code. The synthetic data tests enables the definition of the limitations of the method and to test the sensitivity to different parameters. In a second step, the polarization analysis was applied to two Martian events, to get a first impression if V_s-velocities can be extract from real data. The following section explains the used equations and theory, the different evaluation methods, the tested parameters and the frequency dependency of the polarization analysis.

2-1   Fundamentals

2-1-1   Reflectivity Code

To test the polarization analysis technique, a set of synthetic data was generated using a reflectivity code. In the first phase of this study, a Fortran 77 code (Müller, 1985), (Fuchs and Müller, 1971) was used to efficiently generate multiple seismograms, for different input models. The P-wave arrivals of these seismograms can further be used for the polarization analysis. Because the code is only running on a Linux console and requires a separate text input file, running multiple models turned out to be rather inefficient. To minimize the computational time, an in-house MATLAB®-based reflectivity code was used in a second phase. One of the advantages of the MATLAB®-based reflectivity code is, that the computation focuses on a single ray parameter rather than a range of slownesses and avoids the time consuming inverse tau-p transform.
The usage of a reflectivity code allows a verification of the calculated S-wave velocities because all model parameters are previously known. This gives the option to validate the model and to check, to which parameters the polarization analysis is sensitive to.

2-1-2 Polarization Analysis

Polarization analysis can be used to calculate the frequency-dependent S-wave velocity from the apparent P-wave incidence angle if the slowness p is known . The required angle can be estimated from the particle motion of the first break of a P-wave in vertical (Z) and radial (R) direction. For simplification purposes, we perform the angle estimation in 2D space by initially rotating the horizontal components into the radial direction. The angle is then estimated in the radial-vertical plane. The trigonometric relation of the ratio between the radial $R(t_i)$ and vertical displacement $Z(t_i)$ can be used to estimate the apparent P-wave incidence angle $\bar{i_P}$ using equation 2-1 (Svenningsen and Jacobsen, 2007). It has to be taken into account that this is angle estimation is only valid for linear motion. As an input for the angle estimation, a window over the first break was used, stretching over N samples, as further explained in chapter 2-1-3.

$$\bar{i_P} = arctan \left[\frac{\sum_{i=1}^{N} |R(t_i)| \, |Z(t_i)|}{\sum_{i=1}^{N} |Z(t_i)|^2} \right] \tag{2-1}$$

At the traction-free surface, an incoming P-wave is reflected into a down going P- and a converted, down going SV-wave, leading to a composite particle motion with an apparent, measured incidence angle that differs from the true incidence angle of the incoming P-wave (Hamarbitan and Margrave, 1996). Figure 2-1 illustrates the tilt of the raypath where the near-surface S-wave velocity defines the apparent P-wave incidence angle, in contrast to the true P-wave incidence angle, which depends on the P-wave velocity (Edme and Kragh, 2010). By using the relation that the apparent P-wave incidence angle is twice the true S-wave incidence angle i_S (Knapmeyer-Endrun et al., 2018) and applying Snell's law (Svenningsen and Jacobsen, 2007) the frequency-dependent S-wave velocity V_S can be estimated with equations 2-2 to 2-4:

$$\bar{i_P} = 2i_S \tag{2-2}$$

$$\frac{\sin\left(\frac{1}{2}\bar{i_P}\right)}{V_S} = \frac{\sin\left(i_P\right)}{V_P} = p \tag{2-3}$$

$$V_S \equiv \frac{\sin\left[\frac{1}{2}\bar{i_P}\right]}{p} \tag{2-4}$$

This shows that the polarization analysis is theoretically insensitive to the V_p-velocity, which is one of the major advantages. For the synthetic data, the slowness p and the used ray-parameters were calculated from the input model with the `get_rayparameter.m`-MATLAB® function (Margrave, 1995). For the Martian data, the slowness for the different events were precalculated by the marsquake service (MQS) at ETH Zurich using the latest Martian velocity models and marsquake locations as 0.124 s/km for the event S0235b and 0.125 km/s for the event S1222a.

In a first phase, the polarization analysis was tested using synthetically generated seismic data. The left plot of figure 2-2 shows a whole trace with the particle motion in the Z-direction displayed on the left and the particle motion in the X-direction displayed on the right. The right plot shows a zoom-in into the window over the first break of the trace in the left plot.
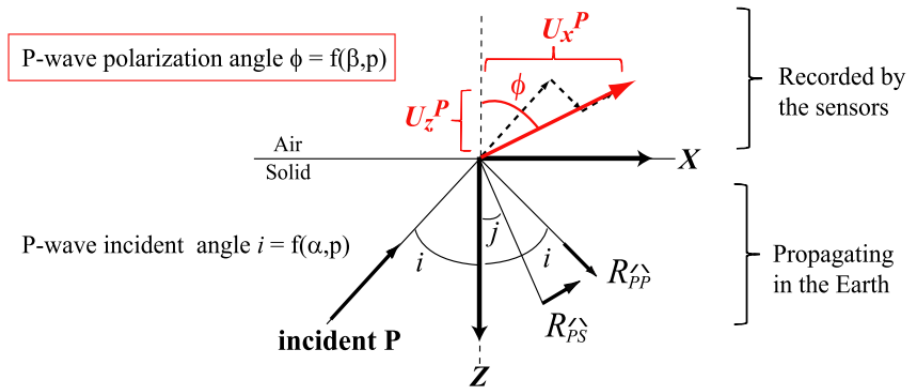
Figure 2-1: At a traction-free surface, the P-wave incidence angle, which is P-wave velocity dependent, differs from the P-wave polarization angle because an incoming P-wave is reflected into a down going P- and a converted, down going SV-wave, leading to a composite particle motion with an apparent, measured incidence angle, which is in the other hand S-wave velocity dependent (Edme and Kragh (2010),Hamarbitan and Margrave (1996))
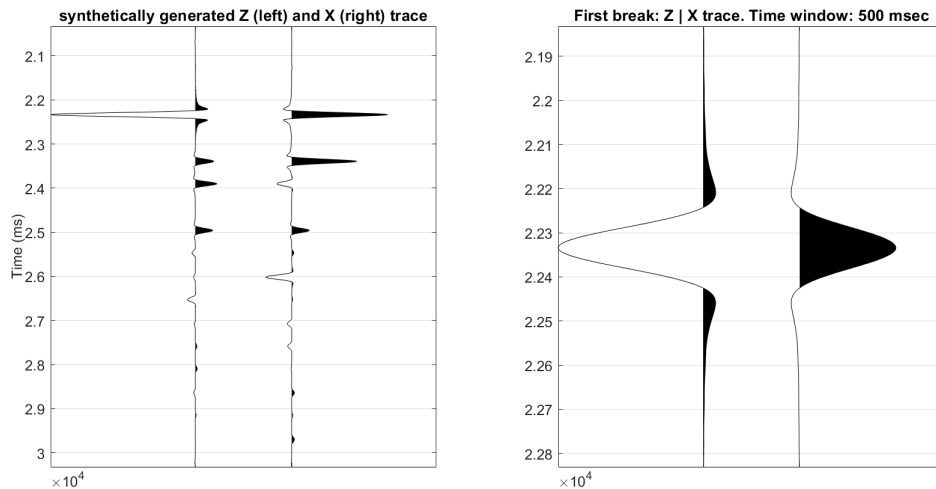
Figure 2-2: Synthetic traces, generated with a reflectivity code. Left figure: Whole seismic trace with the particle motion in Z direction (left) and the particle motion in X direction (right). The source was chosen to be a Gaussian-shaped pulse. Right figure: Window over the first break with a time window of 500 msec.

2-1-3   Windowing

For the velocity calculation, only the windowed first break was used to avoid the interference of other wave types and multiples. Depending on the source frequency or the frequency range which was examined, the window length was adjusted as a range of 1/frequency. This is an important parameter, because if the window length would have been kept constant, it would have not covered the whole wavelet for low frequencies, which is illustrated in figure 2-3, left. For very high frequencies it would have the opposite effect and would include probable later arrivals (Figure 2-3, right). Due to this effect, it is recommended to check
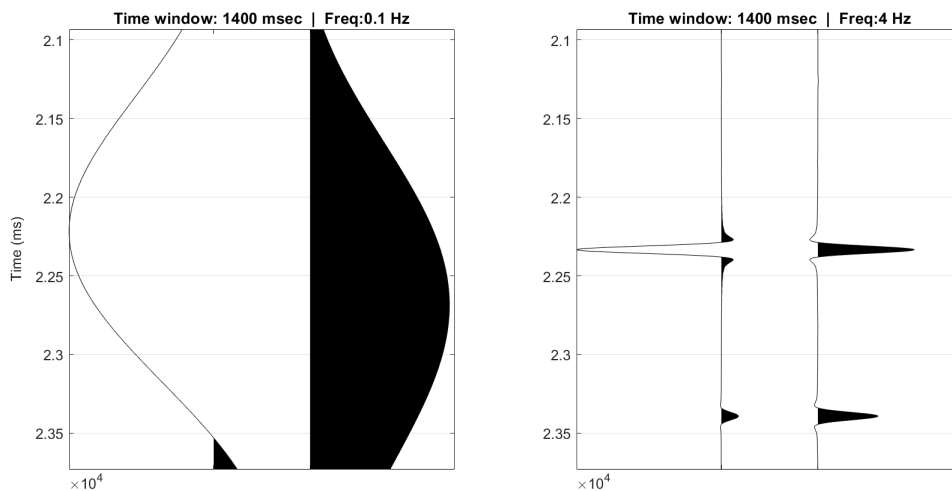
Figure 2-3: Problem of a fixed window length for the polarization analysis. Window length: 1400 ms. The left plot illustrates the problem for too low frequencies. Important information is cut off due to a too short window. The right plot shows when the frequency is too high for a fixed window length, other wave-types with different polarization can get included leading to an erroneous S-wave velocity calculation.

the window-length for the different input frequencies. Additionally to the rule of thumb (1/frequency), the window length has to be cross-checked with the seismogram, to avoid an over- and underestimation of the window length and to guarantee that enough data-points are included. For Martian data, the window had to be adjusted, in a way to exclude the S-wave arrival for low frequencies and to include the whole first break for high frequencies.

2-1-4   Extraction of frequency-dependent Polarization

The description of the selection of the time window above already implies that the polarization analysis is highly frequency-dependent. This raises the question on how to best extract the polarization in a frequency-dependent fashion. One of the chosen option is the variation of the source frequency, which had to be altered before each simulation. This required high computational cost but allowed a broad-band frequency analysis. Another obvious choice would be to bandpass filter the data to narrow frequency bands before extracting the apparent incidence angle from the polarization. To effectively invert the frequency-dependent shear-wave velocity curve, one would need to do this multiple times, once for the simulated data

in each trial model and once for the real data. To fully capture the frequency-dependent behavior in each trial model, it is important to model sufficiently broad-band data, otherwise the extracted polarization becomes less accurate for very high and very low frequencies (at the edges of the modelled bandwidth). This effect can be corrected to a certain point by changing the source time function used in the simulation. Depending on the choice of the source time function, the frequency range is broader, which allows a wider frequency analysis. The three tested sources were a Ricker, a Gaussian and an impulse-source (approximated as a broadband source). The computational cost increases by choosing a source with a broader bandwidth. Figure 2-4 to 2-6 show the different source types, with the frequency range on the left side, the corresponding wavelet on the right. Figure 2-4 show, that the bandwidth of an impulsive source covers a broader bandwidth of frequencies, theoretically an infinite one (only limited by the sampling rate of the output seismograms). The Gaussian frequency bandwidth is, compared to the impulsive one, narrower. The Ricker source exhibits the smallest bandwidth, with the advantage of less computational costs. The advantage of the impulsive source, is that the wavelet is approximately a spike.

Comparing the different sources, a Gaussian source was chosen for this thesis because of its good compromise between a broader bandwidth, a small influence of the wavelet and medium computational cost.

Instead of bandpass filtering the data to different frequency bands, a 1D continuous wavelet transform was used for the real data to extract time- and frequency-dependent polarization properties (The MathWorks, 2006 - 2020).
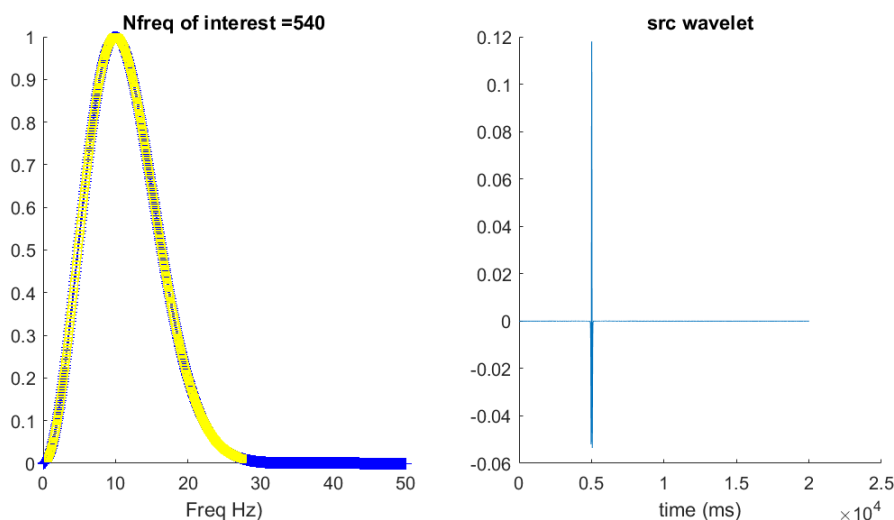
Figure 2-4: Broadband source, which approximates the impulse source. The frequencies ranges from very low to around 30 Hz, which allows a frequency analysis for a broad bandwidth. The wavelet is nearly a spike, which improves the accuracy of the velocity calculation because the wavelet-shape has nearly no impact to the trace.
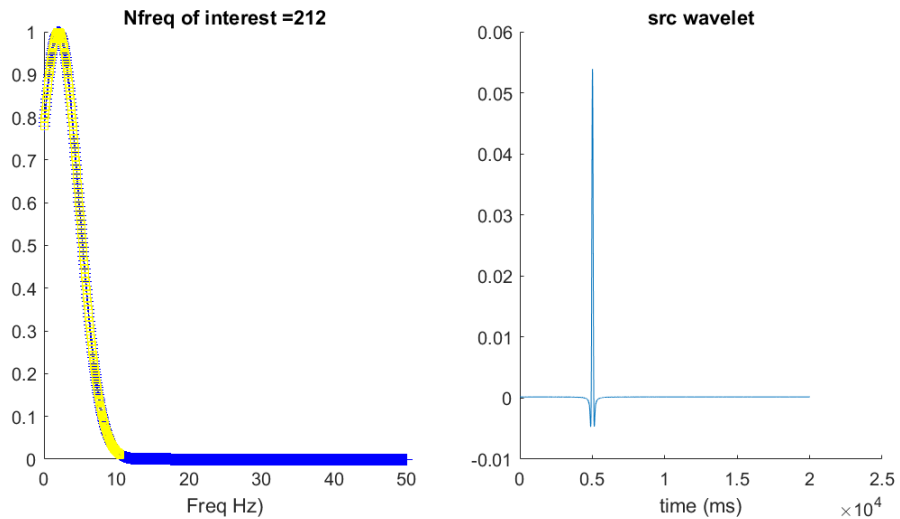
Figure 2-5: Gaussian source. The frequencies range from very low to around 10 Hz, with its maximum around a defined frequency. The wavelet is close to a spike, which can affect the velocity calculation, but not significantly.
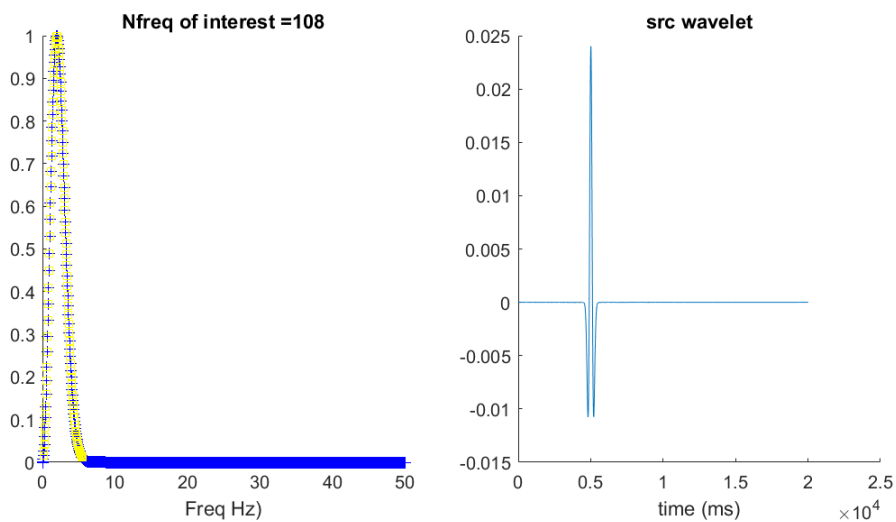

Figure 2-6: Ricker source. The frequencies range from very low to around 6 Hz, which is a quite narrow bandwidth for a frequency filter. The wavelet is a Ricker shape which can influence the velocity calculation due to the wavelet form.

2-2   Input Models for forward Simulations

The input models for the reflectivity code were built to represent real-Earth- and Martian-like conditions. The main input parameters were:

- P-wave velocity, V_p $\left[\frac{m}{s}\right]$

- S-wave velocity, V_s $\left[\frac{m}{s}\right]$

- Density $\left[\frac{kg}{m^3}\right]$

- Source type (Ricker, Gaussian, Broadband)

- Source frequency $[Hz]$

- Number of layer

- Model type (Blocky)

- Slowness $\left[\frac{s}{m}\right]$

- Source depth $[km]$

The models are limited in depth to the first 10 - 20 km because the aim is to refine the velocity changes in this depth range and it is expected that the apparent P-wave incidence angles are only sensitive to the near-surface structure. The model-dependent ray parameters were calculated with the MATLAB®-function get_rayparameter.m (Margrave, 1995). The focus was on a blocky-, two-layer-model, to see under which conditions the frequency-dependent S-wave velocity of the second layer could be extracted. For Mars, the expected S-wave velocities for a depth up to 100 km lie in a range between 2 - 4.5 km/s (Khan et al., 2021). This velocity range was chosen as the framework for the synthetic data testing.

2-2-1   Variation of Model Parameters

The close relationship between wavelength and depth led to two main parameters which were tested for different velocities: The interface depth (thickness of the first layer) and the frequency. Table 2-1 lists the parameters which were calculated for each of the different models. To analyze the sensitivity to the chosen velocities, three different velocity relations were defined. The first one with fixed values for all V_p and a fixed V_s-value for the second layer. The changing parameter was the V_s-value of the first layer. The corresponding velocities are listed in table 2-2. For a second test, the ratio between the V_s- and V_p-values was fixed for the first layer. Table 2-3 shows the corresponding values. The ratio between V_p/V_s of the first layer equals 2. As a third test, a fixed V_p/V_s ratio of 1.4 was chosen for all layers and additionally two velocities were added to cover the whole velocity range (Table 2-4). Further tested models are listed in the appendix chapter A-1-1.
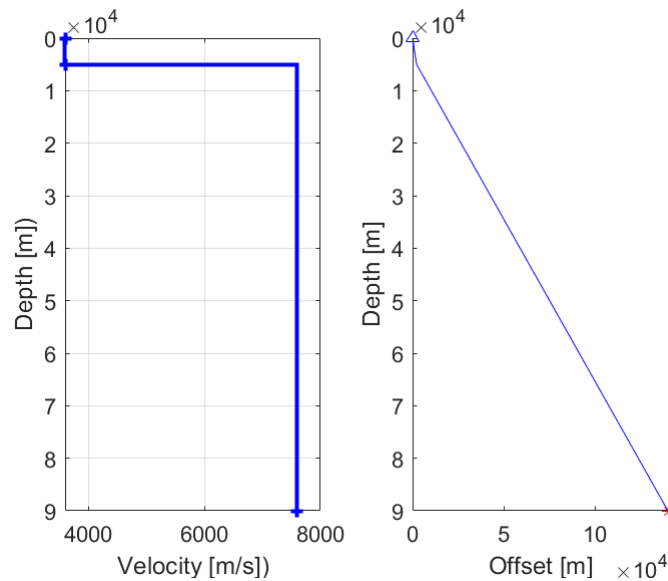
Figure 2-7: Example of a velocity model with two layers and an interface depth of 5 km. Layer 1: $V_s = 1.8$ km/s, $V_p = 3.6$ km/s, $\delta = 2.7$ km/m^3. Layer 2: $V_s = 4.2$ km/s, $V_p = 7.6$ km/s, $\delta = 3.5$ km/m^3. Right plot: Ray-path from the source in 90 km depth.

Table 2-1: Different model parameters for each of the velocity combination for the input model. Layer 1 thickness ranging from 0.2 - 15 km, in steps of 200 m. Source frequency ranging from 0.01 - 6 Hz, logarithmically distributed. The density for the layers was fixed as 2.7 kg/m^3 for layer 1 and 3.5 kg/m^3 for layer 2.

	Range	Step size
Layer 1 thickness [km]	0.2 : 15.0	0.2
Source frequency [Hz]	0.01 : 6.0	log distributed
	Layer 1	**Layer 2**
Density [kg/m^3]	2.7	3.5

Table 2-2: Velocity model 1, where only the V_s-velocity of the first layer is changing for four different combinations. The velocities of V_p and the V_s-velocity of the second layer are fixed.

	V_s **[km/s]**	V_p **[km/s]**
Layer 1	1.0, 1.8, 2.6, 3.4	3.6
Layer 2	4.2	7.6

Table 2-3: Velocity model 2, where the ratio of V_p to V_s is chosen to be constant $= 2$ for the first layer. The velocities of the second layer are fixed.

	V_s [km/s]	V_p [km/s]
Layer 1	1.0, 1.8, 2.6, 3.4	2.0, 3.6, 5.2, 6.8
Layer 2	4.2	7.6

Table 2-4: Velocity model 3, where the ratio of all velocity combination $= 1.4$. 6 different velocity combinations with increasing velocities were tested.

	V_s [km/s]	V_p [km/s]
Layer 1	1.00, 1.60, 2.20, 2.80, 3.20, 3.60	1.40, 2.24, 3.08, 3.92, 4.48, 5.04
Layer 2	1.96, 3.136, 4.312, 5.488, 6.2720, 7.0560	2.7440, 4.3904, 6.0368, 7.6832, 8.7808, 9.8784

2-3 Angle Estimation and Ellipticity

To investigate how the interference of subsequent mode-converted arrivals affects the polarization of the first-arriving P-wave, three different approaches were tested. As a first indicator of the wave polarization, different hodograms were plotted, which show the wave displacement in X and Z direction for a time window around the first break. To evaluate the wave displacement, the incidence angles for the first and second layer were estimated and compared to the hodograms. This enables a first classification of the estimated velocities. As a second indicator, the ellipticity was calculated, to see when the later arrivals start to contaminate the first break of interest, which should be rectilinearly polarized. The ellipticity was computed by calculating the covariance matrix of the X and Z displacement, averaged within the time window, followed by an eigenvalue decomposition (Greenhalgh et al., 2018). For a purely rectilinear arrival, the rank of the covariance drops resulting in a single non-zero eigenvalue (in the case of a pure-state noise-free arrival). The same approach was additionally used to do a more sophisticated angle estimation as a third analysis, whereby the incidence angle was estimated from the principal eigenvector of the covariance matrix. The equations 2-5 and 2-6 show the used angle and ellipticity estimation by eigenvalue decomposition.

The angle and ellipticity estimation in the project was estimated, by calculating the covariance matrix of the polarized waves in a first step, to further extract its eigenvectors and eigenvalues in a second step. The trigonometric relation between the first element of the eigenvector $\boldsymbol{v}_1$ and the second element of the eigenvector $\boldsymbol{v}_2$ can be used to calculate the tilt of the polarization ellipse (Personal communication, Edme (2022)):

$$Angle = \tau = \arctan \left(\frac{\boldsymbol{v}_2}{\boldsymbol{v}_1} \right) \tag{2-5}$$

The ellipticity of the polarized wave was calculated as a combination of its minimum eigenvalue λ_{min} and the maximum eigenvalue λ_{max} (Personal communication, Edme (2022)):

$$Ellipticity = \epsilon = \frac{\sqrt{\lambda_{min}}}{\sqrt{\lambda_{max}}} \tag{2-6}$$

For a purely rectilinearly polarized wave arrival, the ellipticity takes on a value of $\epsilon = 0$ and, a fully circularly polarized arrival would yield an ellipticity of $\epsilon = 1$, or $\epsilon = $ -1 respectively (Taubenschuss and Santolík, 2019). The polarization analysis was done to see how the estimated angles evolve for different first-layer depths and frequency combinations. This helps to understand how the angle transition from the second layer to the first layer works. Calculating the velocities from the angle estimation using the eigenvalue decomposition, helps to confirm the previously estimated velocities using equations 2-1 to 2-4.

2-4 Grid Search and Inversion

As a preparation for the real martian data analysis, an initial grid search and depth inversion was performed for a Martian-like true model, using an RMS misfit functional for the model evaluation. The grid search was set up to loop over different first layer depths as well as different V_s-values and V_p-values for the first layer (Table 2-5). The velocities of the second layer as well as the densities were kept fixed. The grid search was used to describe the model behaviour and to investigate how many local minima will occur in the objective functional of this optimization problem. This should reveal whether or not the depth of the layer interface of the true model can be extracted. The base formula to calculate the misfit was chosen according to Knapmeyer-Endrun et al. (2018) by computing the RMS of the misfit of the observed and modelled apparent S-wave velocities at different periods (or frequencies). To get the best depth inversion, four misfit calculations were tested: The first one by just estimating the frequency-dependent S-wave velocity according to Knapmeyer-Endrun et al. (2018) (equation 2-7). The second one was set up to test the influence of the ellipticity, where the modelled ellipticity was included as a weight according to equation 2-8, meaning that V_S values that were computed from windows exhibiting a low ellipticity were given a higher weight. A third and fourth version of misfit calculation was tested, as a function of the time delay between the P- and PS-arrival and the ratio V_p/V_s. The latter two cases showed significantly less well constrained minima, which is why they were not further used for the inversion.

$$RMS = \sqrt{\sum_{n=1}^{N} \left(v_{obs}(T_n) - v_{mod}(T_n)\right)^2 / (N-1)} \qquad (2\text{-}7)$$

$$RMS_E = \sqrt{\sum_{n=1}^{N} \left(v_{obs}(T_n) - v_{mod}(T_n)\right)^2 \times E / (N-1)} \qquad (2\text{-}8)$$

2-5 Processing of Martian Data

To apply the polarization analysis on real data, mainly two Martian events were analyzed:

- Event S1222a: 04. May 2022

- Event S0235b: 26. July 2019

Table 2-5: Grid search model parameters to calculate the frequency-dependent S-wave velocity v_{mod}. The grid search was built to loop over different first-layer thicknesses, different S-wave velocities for the fist layer as well as different P-wave velocities for the first layer. The V_s and V_p of the second layer, as well as the densities for both layers were set fixed. The RMS misfit summed over different frequencies.

v_{mod}	Range	Step size
Layer 1 thickness [km]	0.2 : 15.0	0.2
V_s **Layer 1 [km/s]**	1.0 : 2.5	0.05
V_p **Layer 1 [km/s]**	2.7 : 4.8	0.10
Source frequency [Hz]	0.01 : 6.0	log distributed
V_s **Layer 2 [m/s]**	2.6	-
V_p **Layer 2 [m/s]**	4.9	-

Table 2-6: Grid search model parameters for the v_{obs} model.

v_{obs}	Range
Layer 1 thickness [km]	9
V_s **Layer 1 [km/s]**	1.7
V_p **Layer 1 [km/s]**	3.7
Source frequency [Hz]	0.01 : 6.0
V_s **Layer 2 [m/s]**	2.6
V_p **Layer 2 [m/s]**	4.9

Because Martian data is not as clean as the synthetic one, they had to be pre-processed before a velocity estimation was possible. Event S1222a was deglitched in a pre-processing step by members of the InSight science team (Scholz et al., 2020). To best visualize event S0235b, a possible bandpass-filter for a frequency range between 0.4 - 0.8 Hz could be applied but was not further used as discussed in chapter 3-0-7. To get a first impression of the polarization of the waves a first 3-C polarization analysis was done with the in-house polarization analysis tool TwistPy written in Python (Personal communication, Sollberger (2022)) to extract the time- and frequency-dependent polarization attributes. In contrast to the provided cwt 1-D wavelet transform, the polarization analysis with TwistPy uses an S-transform and provides information about the ellipticity, the degree of polarization and the directionality. This analysis was done to see which frequencies provide a low ellipticity and how the ellipticity evolves for an increasing time window over the first break. An alternative time frequency polarization analysis was performed, using the continuous wavelet transform, to get an angle and ellipticity estimation with eigenvalue decomposition. The frequencies of the cwt transform, which showed the lowest ellipticities were used to estimate the frequency-dependent S-wave velocity.

Chapter 3

Results

3-0-1 P-Wave Polarization in the Presence of Interfering Arrivals

In a first step, the P-arrivals with their corresponding wave polarization were studied. Figures 3-1 and 3-2 show six different frequency- and first-layer thickness combinations. The red dots in figure 3-1 refer to the P-arrivals, the green dots to the later PS-arrivals (a converted-phase arrival originating at the first layer interface). One of the first observations is, that for the frequency to layer thickness combinations of 0.2 Hz $\longleftrightarrow$ 2 km, 0.2 Hz $\longleftrightarrow$ 5 km, 4 Hz $\longleftrightarrow$ 0.2 km and 4 Hz $\longleftrightarrow$ 2 km, the two arrivals start to overlap, which results in a more elliptical motion, shown in the hodograms in figure 3-2. A rectilinear polarization is indicated, when the horizontal and vertical components are in phase, namely for a low frequency- and thin first-layer-combination (Figure 3-2, top left) as well as for a high frequency- and thick first-layer-combination (Figure 3-2, bottom right). In this case, the wave polarization migrates from the incidence angle of the second layer to the angle of the first layer (from lower to higher frequencies). This is a first encouraging indication that the velocity of the second layer can be estimated for a low frequency and thin first layer combination when the thin first-layer becomes negligible compared to the wavelength. The plots further show, that there is a range in between where the angle did not show a specific direction and hence where the frequency-dependent velocity calculation would not give a good approximation due to the interference of subsequent arrivals. Later arrivals can affect the velocity calculation because the PS-arrival arrives at the seismometer as an S-wave, i.e. the particle motion is pretty much perpendicular to the particle motion of the P-wave. The superposition of the two waves with a slight phase difference leads to an elliptical particle motion. The resulting angle is then not related to the apparent incidence angle of the P-wave and would therefore not lead to a true velocity estimation.

Based on these observations, a first classification into three regimes was performed. The regimes are sketched in figure 3-3 and should illustrate when the extraction of shear wave velocities from the P-wave apparent incidence angle should be possible and when the analysis breaks down. A more sophisticated angle analysis was additionally done by calculating the ellipticity and the angle calculation, as discussed in the chapters 3-0-4 and 3-0-5.

In a next step, the three regimes were defined for a broader bandwidth of source-frequencies

and for a range of varying layer thicknesses (defined in chapter 2-2-1). This analysis showed, that the three regimes could be separated as a function of the time delay between the P- and PS-arrival, briefly explained in chapter 3-0-3. For this project, this time delay is labeled as the approximation variable $\Delta t_{app} = \left(\frac{1}{V_s} - \frac{1}{V_p} \right) \times d$, which itself is a function of the varying layer thickness as well as the P- and S-wavespeeds V_p and V_s of the corresponding layer. Because Δt_{app} is velocity and interface-depth dependent, it changes for the different velocity models. The border between the first regime and the second regime Δt_{app} could be identified to lie between 1.4×1e-4 and 2×1e-4 s over all models and for the tested frequency range of 0.01 - 6 Hz. For values of Δt_{app} below this threshold, a velocity estimation of the first layer was not possible. The regime 1 starts with the lowest defined period of 0.17 s and goes to a maximum period of 1.7 - 11.9 s. This corresponds to a frequency range of 0.08 - 0.6 Hz up to 6 Hz. The found maximum period is velocity dependent and therefore higher, when the corresponding velocity of the first layer is lower. The third regime, where the P-wave polarization angle is sensitive to the velocity of the second layer, expands over the whole range of Δt_{app} but can only be calculated for higher periods. For small Δt_{app}'s the second regime starts at a minimum period of 0.5 - 1.7 s or 0.6 - 2 Hz respectively. It expands for all higher periods up to the maximum defined period of 100 s.
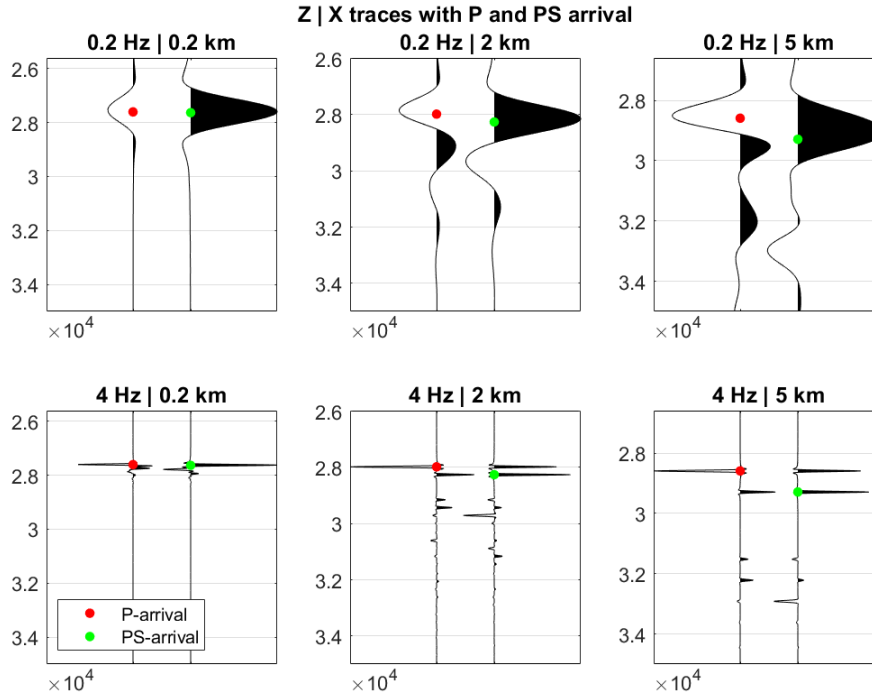

Figure 3-1: P- and PS-arrival for different source frequencies and first-layer thicknesses. Top row: Source frequency of 0.2 Hz with first layer thicknesses of 0.2, 2 and 4 km. Second row: Source frequency of 4 Hz with first layer thicknesses of 0.2, 2 and 4 km. Red dot: P-arrival. Green dot: PS-arrival. Except for the figures top left and bottom right, it can be seen, that the PS-arrival influences the first break and the horizontal and vertical components are not fully in phase. This behaviour is frequency- and interface-depth-dependent.

In between these defined boundaries of the first and third regime, is the second regime. This means for approximation values Δt_{app} lower than $1.4\times 1e\text{-}4$ - $2\times 1e\text{-}4$ s and periods below 0.5 - 1.7 s, no reasonable velocity estimation would be possible using the P-wave polarization angle. The second regime expands for increasing periods and larger approximation values Δt_{app}. It has to be mentioned, that the found boundaries correspond to the defined velocity models 1-3 for this project and can vary depending on the tested model.
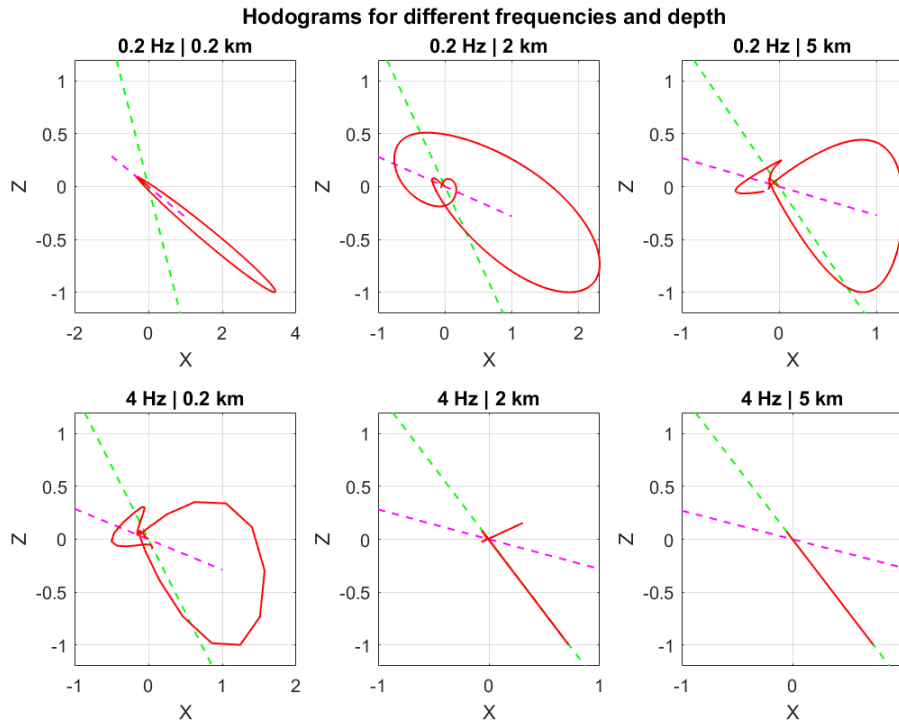

Figure 3-2: Hodograms for three different first-layer thicknesses and two different source frequencies referring to figure 3-1. Green line: Estimated P-wave incidence angle of the first layer. Pink line: Estimated P-wave incidence angle of the second layer. The hodogram align, depending on the layer thickness and frequency, towards the incidence angle of the second layer (top left) or the first layer (bottom right). By comparing the hodograms to the wave-arrivals in figure 3-1 it can be seen, that the angle estimations are plausible when the wavelets are in phase and not disturbed by later arrivals.

3-0-2   Frequency-dependent S-Wave Velocity Estimation

After the definition of the three regimes, the synthetic data testing for the three models was extended to a finer grid to see how the estimated frequency-dependent S-wave velocities change for a wide range of frequencies and layer thicknesses. In a first phase, the velocity estimation was done in a simpler way according to the equations 2-1. A more sophisticated angle estimation followed in a second step according to equation 2-5. The velocity estimations with the two different methods resulted in a comparable velocity output. The following section shows the output of the velocity estimation using the eigenvalue decomposition because of
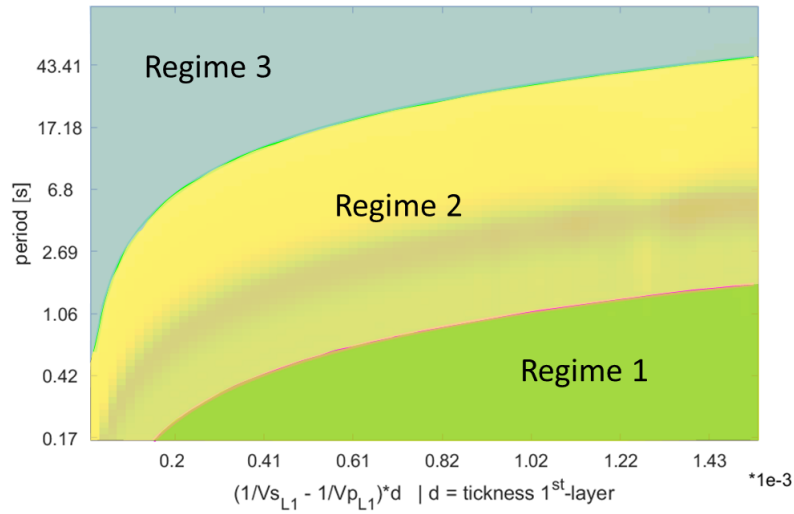
Figure 3-3: 3 Regimes for the tested models. The regime 1 (green) marks the area, where the frequency-dependent V_s-velocity of the first layer can be extracted. The regime 2 (yellow) shows the area where no clear frequency-dependent V_s-velocity can be estimated due to interference of mode-converted phases. The regime 3 (blue) shows the area, where the apparent P-wave incidence angle is sensitive to the velocity of the second layer. The regimes are dependent on the period, the first layer thickness, and the velocity. Empirical borders of these regimes are described in chapter 3-0-3.

its slightly higher accuracy. Figure 3-4 to figure 3-6 show the results for the three different velocity models. The extracted S-wave velocity is plotted as a function of the period and Δt_{app}. The period is calculated as the inverse of the dominant source frequency. The x-axis was defined as a function of the time difference Δt_{app} between the P- and PS-arrival. The color-scale represents the estimated frequency-dependent S-wave velocity. For all models, the velocity of the first layer appears in the low-period range, especially for thicker first layers (bottom right part of the plots). This would correspond to the first regime, as defined in chapter 3-0-1. The second-layer velocity appears for higher periods, especially for thin first-layers, which correspond to the third regime. The second regime, with a non-gradual velocity transition, is also displayed in the plots. For all models the transition between the layers is more clear for generally higher velocities.

For the velocity model 1, only the V_s-velocity of the first layer is changing. Figure 3-4 shows, that the area of the second regime, where a velocity can not be clearly defined, increases for higher V_s-velocities of the first layer (bottom right plot). This illustrates, that a velocity estimation of the first layer is nearly impossible for this parameter setup because it would require a really thick first layer or very low periods. The models 2 and 3 show, that the area of the second regime does not change significantly for different velocity combinations. In contrast to model 1, the two other models (2 and 3) have a fixed, constant ratio between V_p/V_s. This indicates that the velocity estimation could be sensitive to the difference between the V_s and V_p velocity of the layer but remains constant, when the ratio between the two stays the same.

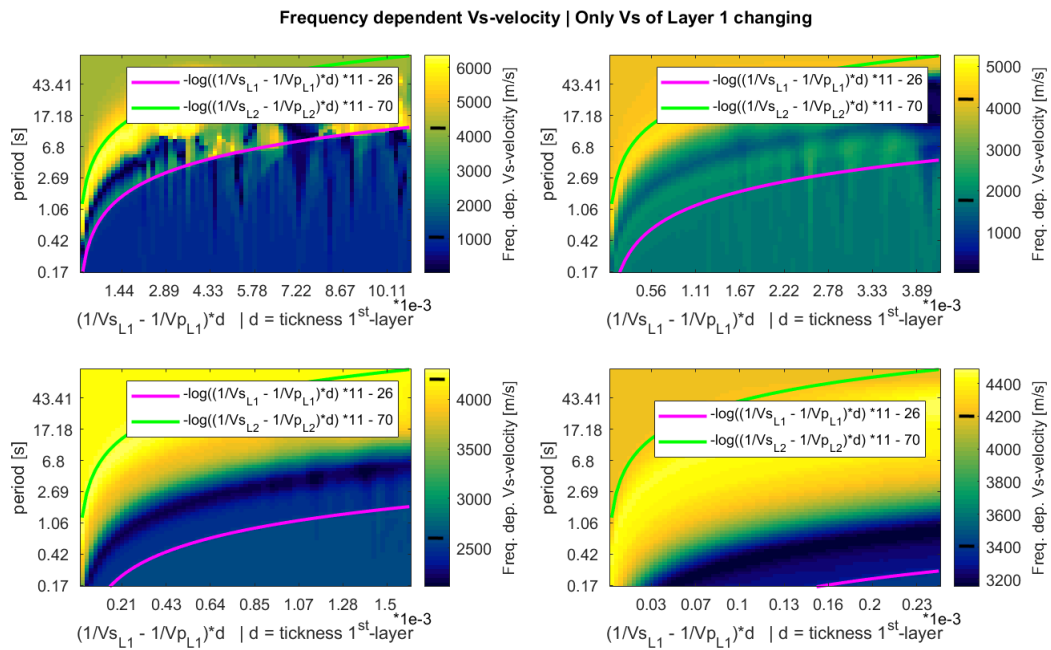**Frequency dependent Vs-velocity | Only Vs of Layer 1 changing**

Figure 3-4: Model 1: frequency-dependent S-wave velocity estimation for a model with only the V_s-velocity of the first layer changing. The corresponding velocities are listed in table 2-2. The black lines in the colorbar mark the reference S-wave velocities of the first and second layer. The bottom right part of the plots approximate the V_s-velocity of the first layer, whereas the top left part of the plots approximate the V_s-velocity of the second layer. The pink and green curves are approximated according to chapter 3-0-3. The curves define the transition between the regimes 1 to 3. For small velocity contrasts the area of the second regime increases towards deeper interface depths and lower periods.
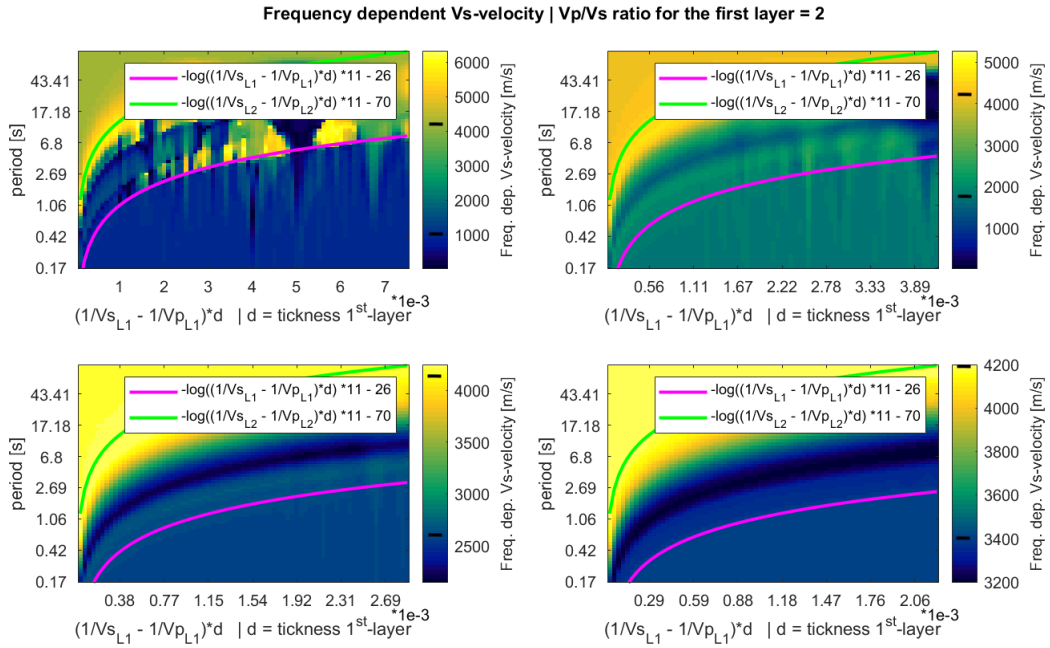
August 5, 2022

Figure 3-5: Model 2: frequency-dependent S-wave velocity estimation for a model where the V_p/V_s ratio of the first layer $= 2$. The black lines in the colorbar mark the reference S-wave velocities of the first and second layer. The corresponding velocities are listed in table 2-3. The velocity distribution follows the same trend as in figure 3-4, with a more stable area for the second regime.
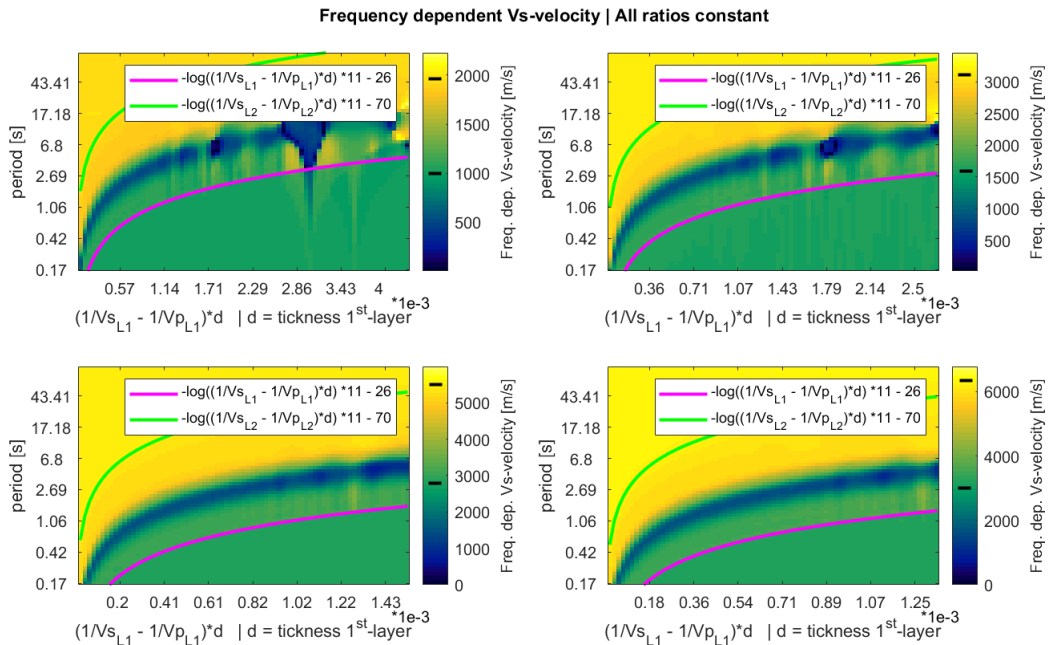

Figure 3-6: Model 3: frequency-dependent S-wave velocity estimation for a model where the V_p/V_s ratios of the first and second layer $= 1.4$. The black lines in the colorbar mark the reference S-wave velocities of the first and second layer. The plot shows four out of six tested velocity combinations for the first layer Vs-velocities: 1, 1.6, 2.8, 3.2 km/s. The corresponding other velocities are listed in table 2-4. The velocity distribution follows the same trend as in figure 3-5.

3-0-3 Approximation Curve between the Sections

All calculated frequency-dependent S-wave velocities in section 3-0-2 show an equal, non-linear trend. To define the transition between the three regimes, an approximation line could be derived as a function of the time difference between the P and PS-arrival (equation 3-1). Because the incidence angle was close to normal for the computed example and hence the horizontal slowness tends to be small ($p \to 0$), the horizontal slowness was neglected for simplification purposes. With the local, vertical S-wave and P-wave slownesses q_S and q_P and $p \to 0$ the following approximation could be done:

$$\Delta t = (q_S - q_P) \cdot d \tag{3-1}$$

$$q_S = \sqrt{\left(\frac{1}{V_s}\right)^2 - p^2} \tag{3-2}$$

$$q_P = \sqrt{\left(\frac{1}{V_p}\right)^2 - p^2} \tag{3-3}$$

$$\Delta t = \left(\sqrt{\left(\frac{1}{V_s}\right)^2 - p^2} - \sqrt{\left(\frac{1}{V_p}\right)^2 - p^2}\right) \cdot d \tag{3-4}$$

$$Approximation = \Delta t_{app} = \left(\frac{1}{V_s} - \frac{1}{V_p}\right) \cdot d \tag{3-5}$$

Here, d is the thickness of the first layer, V_s and V_p the velocities of the first or second layer and Δt_{app} is the approximation derived by setting the horizontal slowness to 0. It was found that the line describes the trend between regime 1 and regime 2 when the velocities of the first layer are implemented. If the velocities of the second layer are used, the trend line follows the transition between regime 2 to regime 3. For plotting purposes in the figures for the velocity and ellipticity, the approximation-curves were adjusted according to the used model, with a logarithmically scaled y-axis.

3-0-4 Ellipticity

To see from which point on the velocity calculations of the layers are accurate, the ellipticity was calculated for all models according to equation 2-6. The ellipticity output of the models 1 and 3 are shown in the figure 3-8 and 3-9. The ellipticities for model 2 are listed in the appendix and are comparable to model 1. The calculated ellipticities range from 0 to 1, whereas 1 indicates a high ellipticity and 0 a linear polarization (Taubenschuss and Santolík, 2019). By comparing the ellipticity with the velocity, it can be seen that the ellipticity follows the same approximation lines. The pink line in the plots for the ellipticity shows, that the line for the first layer velocity precisely separates the area where the ellipticity starts to set in due to the influence of the PS-arrival. The transition for the second layer is less sharp but also follows the trend-line (green). This indicates, that the ellipticity is highly influenced by

the time difference between the P- and PS-arrival (chapter 3-0-3). The previously discussed regime 2 can also be defined for the ellipticities, appearing as an increase in ellipticity. The regimes 1 and 3 emerge due to low ellipticity values. The approximation lines were used to define an ellipticity threshold where a reliable velocity estimation should be possible. It was found, that for an ellipticity of 0.2, the whole area of the second regime is excluded (figure 3-7). The area is framed by the approximation lines. This threshold is valid for all tested models.

Model 1 overall shows lower ellipticities in the second regime for higher V_s-velocities (bottom right plot, figure 3-8). Model 3 shows a relatively similar ellipticity behaviour for all velocity combinations, with an ellipticity jump after the approximation line for the first layer velocity. This suggests that the ellipticity behaviour remains the same, if the ratios between the velocities are constant. The important learning for the ellipticities over all models is, that the velocity calculation gets inaccurate for ellipticities > 0.2. This value can be further used as a threshold and indicator to define the accurateness of the velocity calculation for martian data.
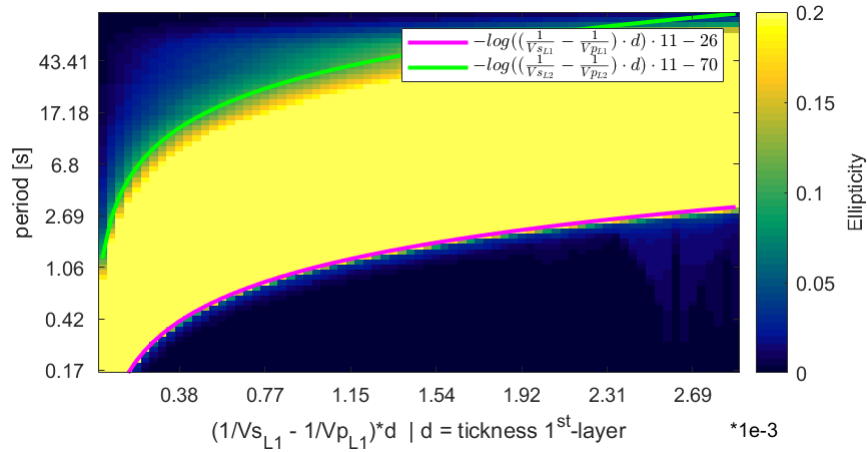

Figure 3-7: Ellipticity threshold of 0.2. The threshold of 0.2 excludes the whole area of the second regime, where no accurate velocity estimation is possible. The area is framed by the approximation lines, defined in chapter 3-0-3 and therefore depending on the arrival of the PS-waves.
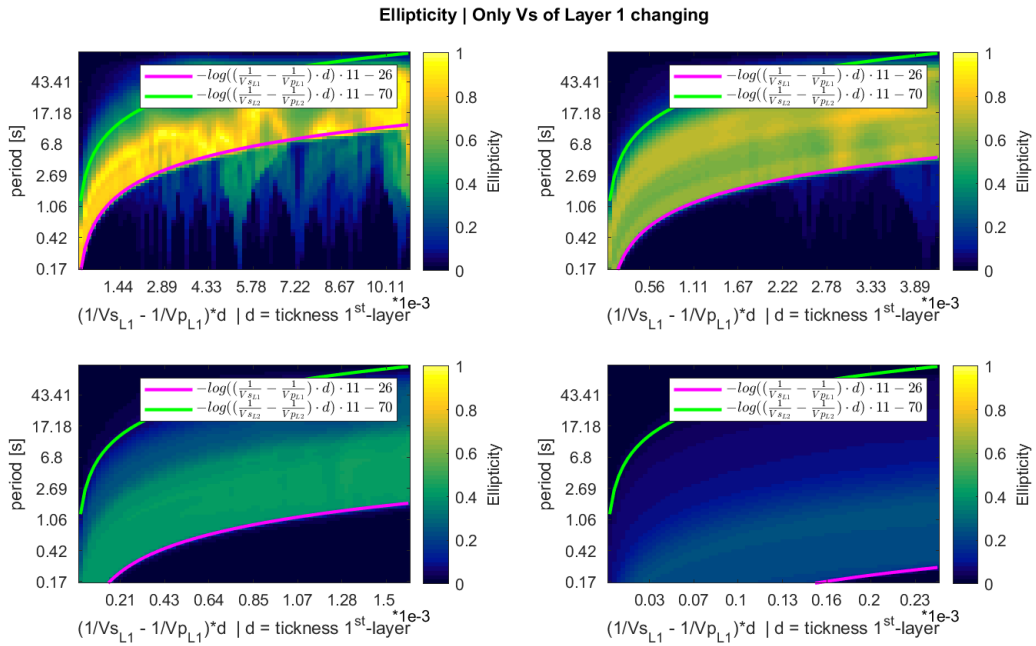
Ellipticity | Only Vs of Layer 1 changing

Figure 3-8: Ellipticity for the velocity model 1. The bottom right plot, where the velocity contrast of the first layer between V_s and V_p is small, the ellipticities are overall lower, than for higher velocity contrasts (top left). The 3 regimes are clearly shown also in the ellipticity plot. The areas with a very low ellipticity (bottom right and top left corner) correspond to the areas, where the frequency-dependent S-wave velocity could be well approximated.
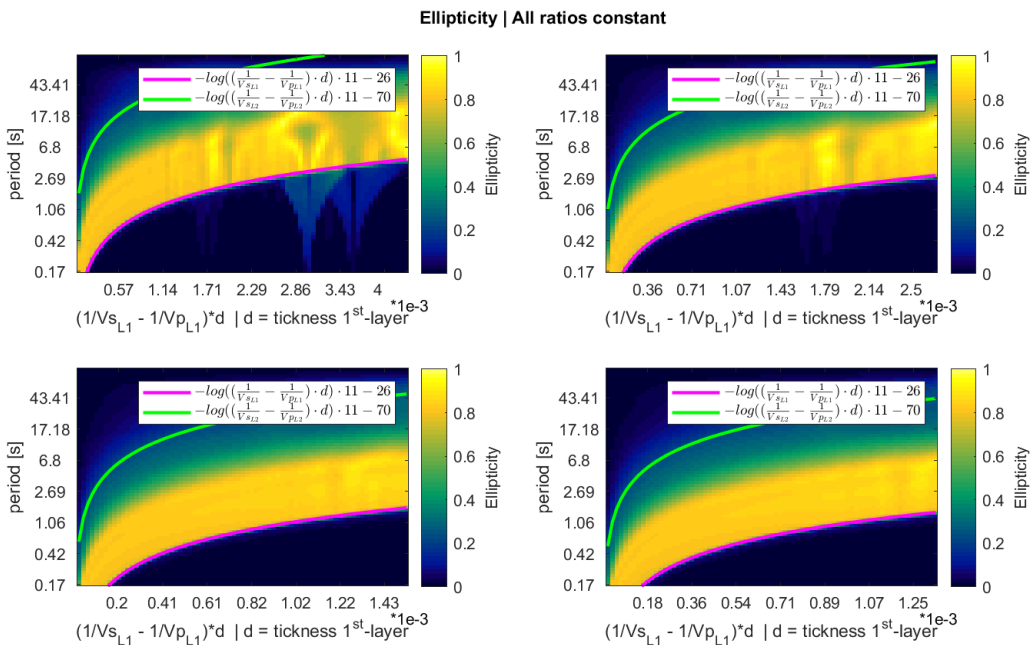
Ellipticity | All ratios constant

Figure 3-9: Ellipticity for the velocity model 3. The ellipticity follows the previously defined 3 regimes, with a relatively sharp transition between the first and second regime and a more gradual transition between regime 2 and 3. The regimes are separated by the green and pink trend-lines. The ellipticity in regime 2 increases drastically due to the influence of the PS-arrival and leads to wrong velocity estimations.

3-0-5   Angle Analysis

To get a deeper understanding of the calculated velocities derived from the apparent P-wave incidence angles, a separate analysis on the apparent incidence angle was performed. The focus laid on the the angle transition between the first and the second layer and to show if the transition is gradual. The angle outputs are listed in the appendix A-2-2. Like the velocity outputs, the angle estimations show the previously identified three regimes (chapter 3-0-1). For the regime 1 and 3 the estimated polarization angle remains constant with a gradual transition into the middle regime 2. In the center part of regime 2 a random jump to non-plausible values appears. This effect was observed in all tested models and indicates that the angle transition in the second regime is not gradual. A comparison of the apparent incidence angle with the ellipticity suggests a potential explanation that the increased ellipticity, due to the influence of the PS-arrival, could cause the observed instability in the estimation of the incidence angle. By comparing the angle with the velocities, it could also be seen, that already a slight change in the angle estimation leads to completely wrong velocity. This is displayed in the plots for the areas in regime 2, where the color range just slightly differs from the bottom right and top left corner.

3-0-6   Gridsearch and Inversion

To investigate whether an inversion of the extracted frequency-dependent shear-wave velocity curves for near-surface velocity profiles was feasible, a simple grid search optimization was performed with data from a true model that was representative for the expected crustal structure at the InSight landing site. The misfits were computed according to equations 2-7 and 2-8. The grid-search should give an idea on how well-behaved the objective function of this inversion problem is in terms of non-uniqueness (multiple potential local minima) and model parameter trade-off. The plots 3-10 and 3-11 show the misfit calculation for varying V_s-values and varying first layer thicknesses, always for a constant V_p value. The true model v_{obs} had a V_p-value of 3700 m/s and a V_s-value of 1700 m/s with an interface depth at 9 km, marked in the plots with a red dot. The contour line defines the area of the lowest 10% of the misfit values, to compare the misfit calculation with the ellipticity implemented and without it. For all V_p values, the 10% area includes the v_{obs} point, even though the misfit calculation is not totally insensitive to various V_p-values, like they should, following the theory. All figures show a relatively well constrained single minimum value, especially for the case where the V_p value equals the true model. For both cases the misfit is larger for V_s-velocities lower than the true model and increases for larger first layer thicknesses. V_s-velocities higher than the observed model show a more gradual misfit and for the case where the ellipticity is included (figure 3-11) it remains nearly constant. The two cases, with the ellipticity included and the case without the ellipticity, were compared by comparing the area which is constrained by the 10% line. The area for the misfit, where the ellipticity is not included, was 2-3 times smaller than the case with the ellipticity. This leads to the conclusion, that a misfit calculation without the ellipticity included is recommended. By comparing figure 3-10 with figure 3-11 it can be seen, that the low misfit area (dark blue) does more spread over the model range, when the ellipticity is included. This indicates, that the ellipticity is an important factor but it is not the only significant value for a proper inversion.
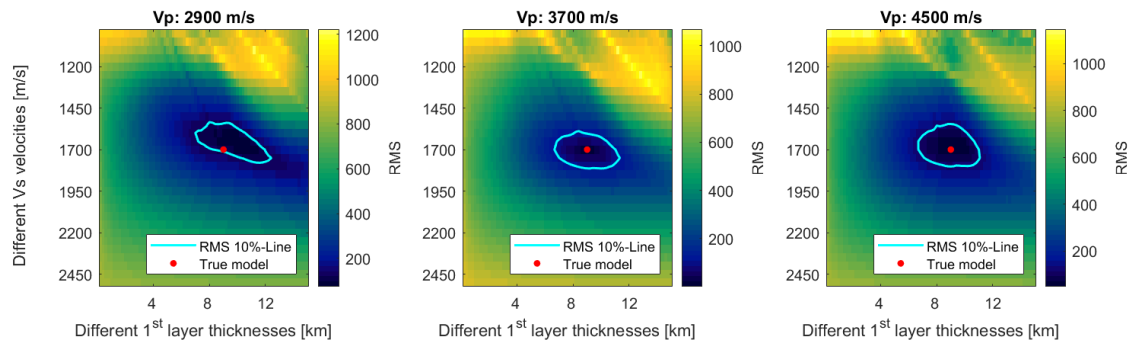
Figure 3-10: RMS misfit calculation without taking the ellipticity into account (equation 2-7). The misfit is calculated for various V_s-velocities and varying first layer thicknesses according to table 2-5. The blue line shows the area where the misfit is below 10% of the maximum value. The red dot indicates the true model. The misfit shows one local minima for all velocity and depth calculations, whereas the misfit is larger for low V_s velocities.
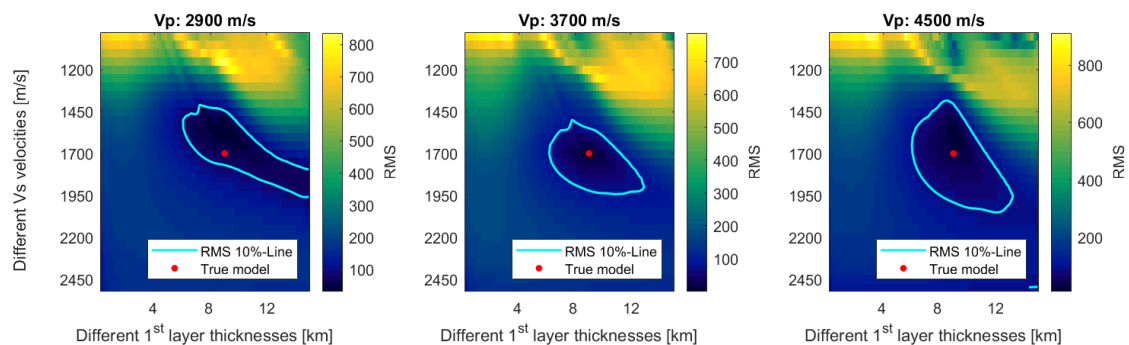

Figure 3-11: RMS misfit calculation with taking the ellipticity into account (equation 2-8). Compared to the misfit without the ellipticity the low misfit values spread more over the modelling range and are less well constrained. The 10% area is 2-3 times larger than the one without the ellipticity, what shows that the depth inversion is better defined for a misfit calculation without the ellipticity.

3-0-7   Application to Martian data

The synthetic data tests showed, that the velocity estimation based on the P-wave polarization angle is sensitive to the influence of other wave-types. Also, the frequency content, thickness of the layer and the velocity of the layers play an important role. A major learning form the synthetic tests is, that some frequency-dependent S-wave velocities can only be retrieved, when the polarization is linear and interference of the mode-converted PS arrival does not impact the calculation of the apparent P-wave incidence angle. For this reason, a detailed polarization analysis of the P-wave first arrival was performed for the two events recorded on Mars in order to identify the frequencies, where accurate S-wave velocities can be extracted. To do so a 1D continuous wavelet transform (The MathWorks, 2006 - 2020) was applied to the data for each event. Polarization properties were then computed on the time-frequency representation (CWT) of the multi-component time series. Figures 3-12 and 3-13 show the ellipticity of the first-arriving motion as a function of frequency. Only shear wave velocities for frequencies showing an ellipticity smaller than 0.2 were estimated. For the event S1222a, four frequencies were picked, where the ellipticity is minimal and below the previously defined threshold of 0.2. The corresponding frequencies are: 0.21, 0.44, 0.82, 1.43 Hz. These frequencies were further used to estimate the frequency-dependent S-wave velocity for this event. Other frequencies were not taken into account because their ellipticity was too high. A potential explanation for the high ellipticity values at high frequencies could be an increasing contribution of scattered energy.
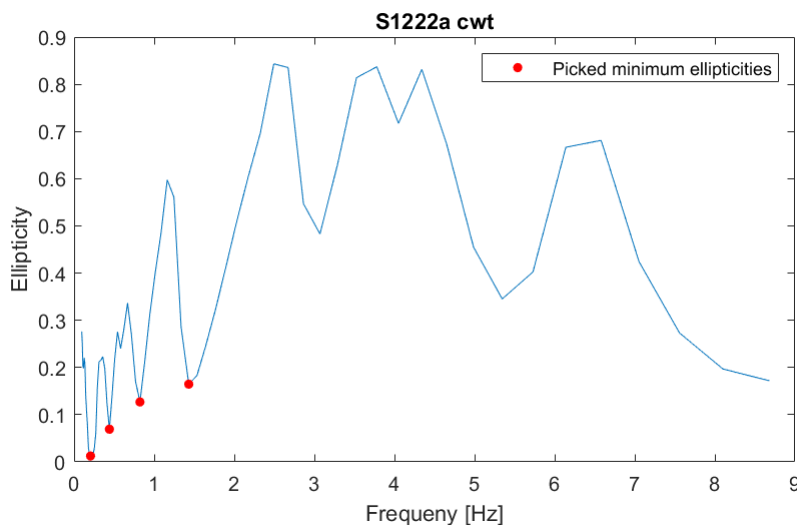

Figure 3-12: Ellipticity of the first-arriving motion as a function of frequency for the event S1222a. The four minima of the ellipticity were picked at the following frequencies: 0.21, 0.44, 0.82, 1.43 Hz.

Figure 3-14 shows hodograms of the first arriving motion for four frequencies extracted with the CWT for the S1222a event. The corresponding time-windowed traces are shown in figure 3-15. In Figure 3-14, the best-fitting polarization ellipses extracted by an eigenanalysis of the covariance matrix are plotted in magenta. The frequencies of 0.82 and 0.44 Hz show an ellipticity smaller than 0.2 but estimated incidence angle is relatively large, potentially because the PS wave is introducing motion into the horizontal component. Therefore, these
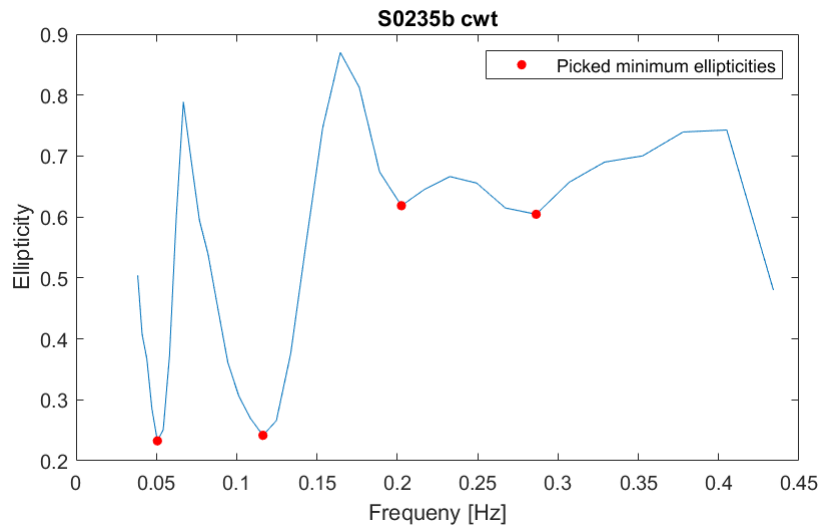
Figure 3-13: Ellipticity of the first-arriving motion as a function of frequency for the event S0235b. The frequencies where the ellipticity is minimal were picked as: 0.05, 0.12, 0.20 and 0.29 Hz. None of the ellipticity values lie below the threshold value of 0.2 and are therefore not suitable for a following frequency-dependent S-wave velocity estimation.

traces were not further used for a velocity estimation. The frequency of 1.43 Hz with an ellipticity of 0.13 and an estimated apparent incidence angle of 38.7 degrees could be reliable and would lead to an S-wave velocity of 2664 m/s. The most convincing results were obtained at a frequency of 0.21 Hz. With an ellipticity of 0.01 the P-wave motion at this frequency is nearly rectilinearly polarized and the angle of 35.1 degrees could be reasonable. The V_s-velocity for this frequency would then be 2451 m/s.

For the second event S0235b, a first evaluation of the ellipticity versus frequency showed, that all ellipticities were above 0.2 and would thus not yield any reasonable estimates of the shear wave velocity. The same problem was also observed for other tested low-intensity Martian seismic events, which are not listed in this thesis. To exclude the noise of the data, which is probably the reason for the high ellipticity, a frequency filter was applied in a first step. By evaluating the filtered data, it could be seen, that the ellipticity values were going down, but the cwt output, as well as the wave polarization were too monochromatic for a following velocity estimation. Additionally to that, the filtering excludes certain frequency bands, which would be needed for a reasonable polarization analysis. Therefore the unfiltered P-wave arrival was used, even though the minimum ellipticities were above 0.2 (figure 3-13). The picked frequencies, where the ellipticity is minimal for that event, are: 0.05, 0.12, 0.2 and 0.29 Hz. The corresponding seismic traces are shown in the appendix chapter B-1-1. The hodograms and best-fitting polarization ellipses are shown in figure 3-16. The plot illustrates the problem that the wave polarization, even for the minimum observed ellipticities, does not follow a clear trend and the estimated angles seem completely off. Therefore, a velocity estimation would not lead to a reasonable output and was not further calculated.
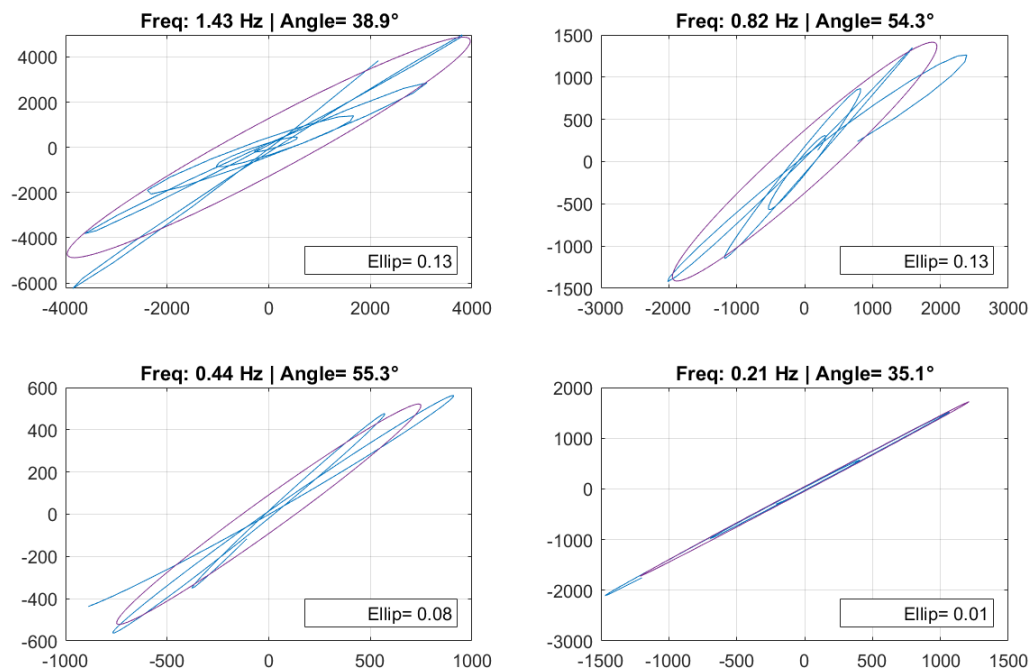
Figure 3-14: Hodograms of the first-arriving motion for the Martian event S1222a: 04. Mai 2022 (InSight Mars Data Service, 2022). The best-fitting polarization ellipses extracted by an eigenanalysis of the covariance matrix are plotted in magenta. The picked frequencies where the ellipticity is minimal are 1.43, 0.82, 0.44 and 0.21 Hz (top left to bottom right). The bottom right plot shows an ellipticity of 0.01, which is nearly linear polarized. This would allow a reliable angle estimation of 35.1 degrees and would correspond to an frequency-dependent S-wave velocity of 2451 m/s. The top left plot for a frequency of 1.43 Hz and with an ellipticity of 0.13 could be potentially used for a velocity estimation, where the frequency-dependent S-wave velocity would be 2664 m/s. The top right and bottom left plot show a low ellipticity but a relatively large angle, probably because the PS wave is boosting the horizontal component. Therefore a velocity estimation would not be trustworthy.
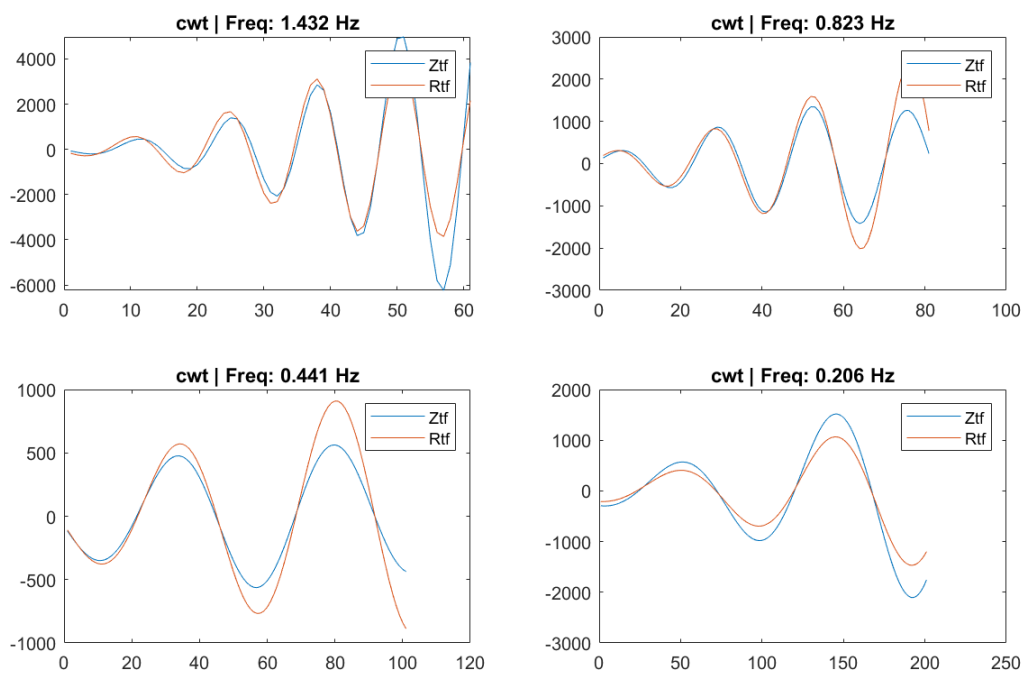
Figure 3-15: Horizontal and vertical component seismograms of the first-arriving motion for the event S1222a: 05. Mai 2022 (InSight Mars Data Service, 2022). The chosen frequencies belong to the frequency bands where the ellipticity is minimal for that event. Because the seismograms in Z- and R-direction are predominantly in phase, the ellipticities show accordingly low values (figure 3-14). The window length is chosen according to the wavelength of the frequency and adjusted to ensure a minimum amount of data points.
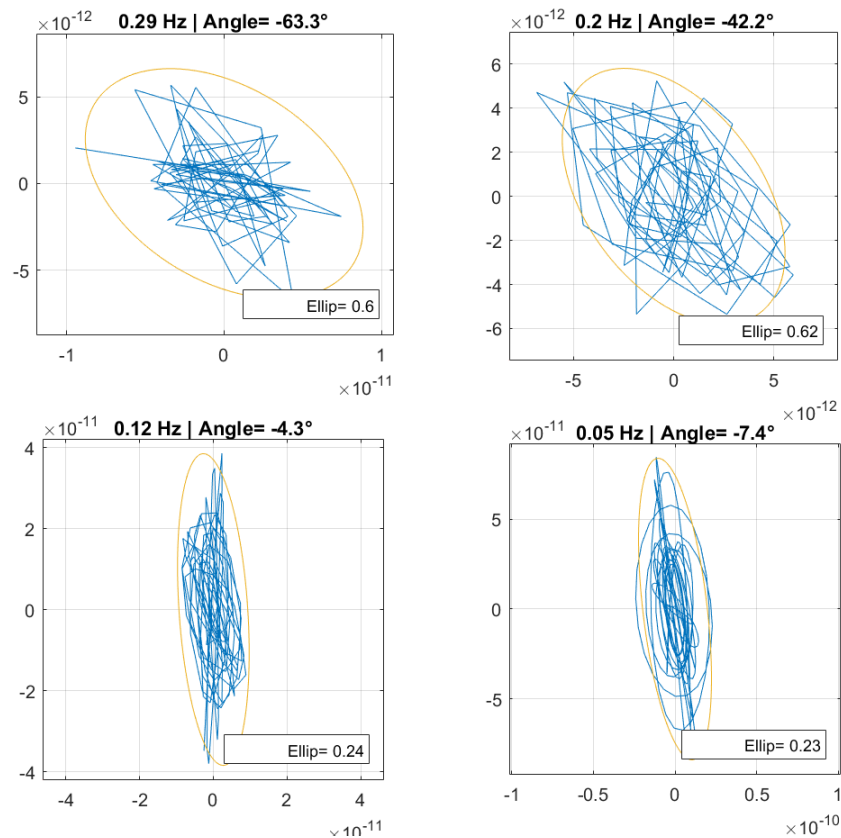
Figure 3-16: Hodograms and best-fitting polarization ellipses for the first motion recorded during the event S0235b: 26. June 2019 (InSight Mars Data Service, 2022). The picked frequencies for the event are 0.29, 0.20, 0.12, 0.05 Hz (top left to bottom right). Due to the low signal-to-noise ratio the particle motion appears to be random (isotropic polarization) leading to a relatively high ellipticity (> 0.2). Therefore, the angle estimation and the corresponding velocity estimation would probably not show the true representation of the structure.

Chapter 4

Discussion and Conclusion

Polarization analysis of the first-arriving P-wave motion provides the opportunity to extract subsurface information in the form of a frequency-dependent S-wave velocity. The synthetic data tests, which covered a large part of this thesis, showed that for a two-layer model, frequency-dependent S-wave velocities can be extracted that match with the true S-wave velocities of the two layers at specific frequencies. The success of this velocity estimation is limited by various parameters like the ellipticity of the first-arriving motion, interference of mode-converted phases and the signal-to-noise ratio of the data .

The evaluation of the simple two layer model showed, that S-wave velocity extraction of the first layer just below the receiver is possible for a time difference between the P- and PS-arrival (Δt_{app}) larger than 1.4×1e-4 - 2×1e-4 s. The velocity of the second layer can in contrast only be extracted, when the frequency is below 0.6 - 2 Hz for the whole range of the tested Δt_{app}. This indicates that if a relatively thin first layer is present, the estimation of the velocity of the second layer is possible. For the tested model space, where the layer thicknesses varied between 0.2 to 15 km this required already quite low frequencies for most of the tested models, predominantly frequencies below 1 Hz. The possibility to reach even deeper layers than the second one, should be further investigated but would require even lower frequencies and a thin first and second layer thickness.

For the extraction of frequency-dependent polarization angles, the time window length used for polarization analysis has to be adjusted according to the the dominant period at each frequency. For very low frequencies, this would require a very long time window, which might include interfering arrivals that potentially impact the polarization leading to biased values of the shear wave velocity. This is why the extraction of shear wave velocities at very low frequencies is expected to be challenging.

The synthetic tests also showed a regime where the velocities could not be estimated properly using the proposed technique. Here, the interference of the mode-converted PS phase originating at the layer boundary leads to a random jump in the estimated polarization angle. This effect could be identified by separately looking at the P-wave arrivals for varying interface depths using reflectivity code simulations. The interfering PS-arrival has a strong influence on the ellipticity, where at least values below 0.2 are required to extract the correct velocity information.

In summary, the evaluation of different models showed that the velocity calculation can be split into three regimes. The first one, where the velocity of the first layer can be extracted. A second one, where no specific velocity can be defined. And a third regime, where the velocity of the second layer can be calculated. The three regimes can be separated as a function of the time difference between the P and the PS arrival in the following way: $\Delta t_{app} = \left(\frac{1}{V_s} - \frac{1}{V_p} \right) \times d$. It includes the V_p- and V_s-velocities of either the first or the second layer, as well as the depth, and indicates the point from which a reasonable velocity estimation should be possible. For the analysis, only waves arriving with a relatively small horizontal slowness were considered (meaning that the incidence of the P-wave is close to vertical). This should be kept in mind when transferring the knowledge gained here to real data.

The ellipticity of the first-arriving P-wave motion was found to be a good first indicator to estimate if the extracted frequency-dependent S-wave velocities can be trusted. It was possible to define an empirical upper limit threshold of 0.2 for the ellipticity. For ellipticities larger than that, the velocity cannot be estimated accurately anymore. Frequency bands with a smaller ellipticity than 0.2 can possibly be used for a velocity estimation. The value of 0.2 was defined by the evaluation of different models where it marks the transition of the regimes 1 and 3 into the 2nd regime.

An attempt to invert the frequency-dependent S-wave velocity curves for near-surface structure using a grid search algorithm showed the varying sensitivity of the model for different V_s- and V_p-values versus the thickness of the first layer. For all models, the chosen RMS misfit showed one local minima, where the depth of the interface could be accurately extracted for a simple synthetic example. The misfit is larger for V_s-values lower than the true model and gradually increases for V_s-values higher than the true model. By comparing a misfit calculation with and without the ellipticity implemented, it could be shown, that the ellipticity is a good indicator for the accuracy of the velocity calculation but the misfit with just the frequency-dependent S-wave velocity gives a better constrained observed global minimum. To invert actual Martian data, the misfit calculation should be extended to a wider range of parameters i.e., using more layers to represent a near-surface velocity gradient with depth. Potentially other misfit functions than the RMS misfit could be tested to find the best-fitting model.

The application of the polarization analysis scheme to the two Martian events did confirm the findings from the synthetic data tests. For the event S1222a, two S-wave velocities could be estimated as 2451 m/s and 2665 m/s at frequencies of 0.2 Hz and 1.4 Hz, respectively. The velocity extraction for that event at other frequencies was not possible because either the ellipticity was too high or the estimated incidence angle was not reasonable. A potential explanation for that could be the interference of mode-converted arrivals, as shown in the synthetic data tests. However, the two estimated velocities seem to be reasonable and have to be cross checked with velocity estimations obtained from other methods. It has to be mentioned that the S-wave velocity estimation for this event was only possible because of its large magnitude and thus high signal-to-noise ratio and its broad frequency content compared to other marsquakes. The evaluation of the second event S0235b and also other low-intensity events showed, that the velocity estimation was not possible, due to too low signal-to-noise ratios.

The various tests conducted within this thesis suggest that it is likely that frequency-dependent S-wave velocities can be extracted from real data. A first basic grid-search optimization showed that for a synthetic two-layer model the interface depth can be estimated

by inverting the frequency-dependent S-wave velocity curve. However, for real data, a few parameters should be considered to ensure that the polarization analysis is stable. Events with a high signal to noise ratio are needed and the ellipticity of the first break has to be as small as possible (see the empirically found threshold of < 0.2) in order to agree with the theory of a rectilinearly polarized P-wave motion.

Bibliography

P. Edme. Personal communication, matlab function; `get_pol.m`, June 2022.

P. Edme and E. Kragh. Near-surface s-wave velocity estimation from p-wave polarization analysis. In *72nd EAGE Conference and Exhibition incorporating SPE EUROPEC 2010*, pages cp–161. European Association of Geoscientists & Engineers, 2010.

ETHZ. Die eth zürich auf dem mars, [mission], December 2021. URL http://www.insight.ethz.ch/de/mission/.

K. Fuchs and G. Müller. *Computation of Synthetic Seismograms with the Reflectivity Method and Comparison with Observations*. Geophys. J. R. astr. Soc. **23**, 417-433, Geophysical Institute, Universtiy of Karlsruhe, Karlsruhe, West Germany, 1971.

S. Greenhalgh, D. Sollberger, C. Schmelzbach, and M. Rutty. Single-station polarization analysis applied to seismic wavefields: A tutorial. *Advances in Geophysics*, 59:123–170, 2018.

N. S. Hamarbitan and G. F. Margrave. An investigation of the free surface effect. Technical report, Tech. rept. University of Calgary, Canada, 1996.

M. Hobiger, M. Hallo, C. Schmelzbach, et al. The shallow structure of Mars at the InSight landing site from inversion of ambient vibrations. *Nature Communications* **12**, 13(6756), 2021. doi: https://doi.org/10.1038/s41467-021-26957-7.

S. InSight Mars Data Service. SEIS raw data, Insight Mission. IPGP, JPL, CNES, ETHZ, ICL, MPS, ISAE-Supaero, LPG, MFSC., January 2022. URL https://doi.org/10.18715/SEIS.INSIGHT.XB_2016.

A. Khan, S. Ceylan, M. van Driel, D. Giardini, P. Lognonné, H. Samuel, N. C. Schmerr, S. C. Stähler, A. C. Duran, Q. Huang, et al. Upper mantle structure of mars from insight seismic data. *Science*, 373(6553):434–438, 2021.

B. Knapmeyer-Endrun, S. Ceylan, and M. van Driel. Crustal S-Wave Velocity from Apparent Incidence Angles: A Case Study in Preparation for InSight. *Space Science Reviews* **214**, 40(83), 2018. doi: https://doi.org/10.1007/s11214-018-0510-9.

G. Margrave. Matlab function; `get_rayparameter.m`, crewes project, June 1995.

G. Müller. *The reflectivity method: a tutorial.* Geophysics **58**, 153-174, Institute of Meterology and Geophysics, University of Frankfurt, Feldbergstr.47, 6000 Frankfurt, 1985.

NASA. Insight's landing site: Elysium planitia, January 2022a. URL https://www.nasa.gov/image-feature/jpl/pia22232/insight-s-landing-site-elysium-planitia.

NASA. Insight lander, January 2022b. URL https://mars.nasa.gov/insight/spacecraft/about-the-lander/.

NASA. Insight mission overview, January 2022c. URL https://mars.nasa.gov/insight/mission/overview/.

NASA. Insight will take the 'vital signs' of mars, January 2022d. URL https://mars.nasa.gov/insight/mission/science/overview/.

J.-R. Scholz, R. Widmer-Schnidrig, P. Davis, P. Lognonné, B. Pinot, R. F. Garcia, K. Hurst, L. Pou, F. Nimmo, S. Barkaoui, et al. Detection, analysis, and removal of glitches from insight's seismic data from mars. *Earth and Space Science*, 7(11):e2020EA001317, 2020.

D. Sollberger. Personal communication, python package; twistpy, April 2022.

S. C. Stähler, A. Khan, W. B. Banerdt, et al. Planetary Science. [Seismic detection of the martian core]. *Science* **373**, 6(6553):443–448, 2021. doi: 10.1126/science.abi7730.

L. Svenningsen and B. H. Jacobsen. Absolute S-velocity estimation from receiver functions. *Geophysical Journal International*, **170**(6):1089–1094, 2007. doi: 10.1111/j.1365-246X.2006.03505.x.

U. Taubenschuss and O. Santolík. Wave polarization analyzed by singular value decomposition of the spectral matrix in the presence of noise. *Surveys in Geophysics*, 40(1):39–69, 2019.

I. The MathWorks. Cwt continuous 1-d wavelet transform, 2006 - 2020.

Appendix A

Method

A-1   Model

A-1-1   Additionally tested Velocity Models

Table A-1: Velocity model 4, where the ratio of all velocity combination = 1.2. 6 different velocity combinations with increasing velocities were tested.

	Vs [km/s]	Vp [km/s]
Layer 1	1.00, 1.20, 1.40, 1.60, 1.80, 2.00	1.4000, 1.6800, 1.9600, 2.2400, 2.5200, 2.8000
Layer 2	1.9600, 2.3520, 2.7440 3.1360, 3.5280, 3.9200	2.7440, 3.2928, 3.8416, 4.3904, 4.9392, 5.4880

A-2   Results

A-2-1   Ellipticity for Model 2
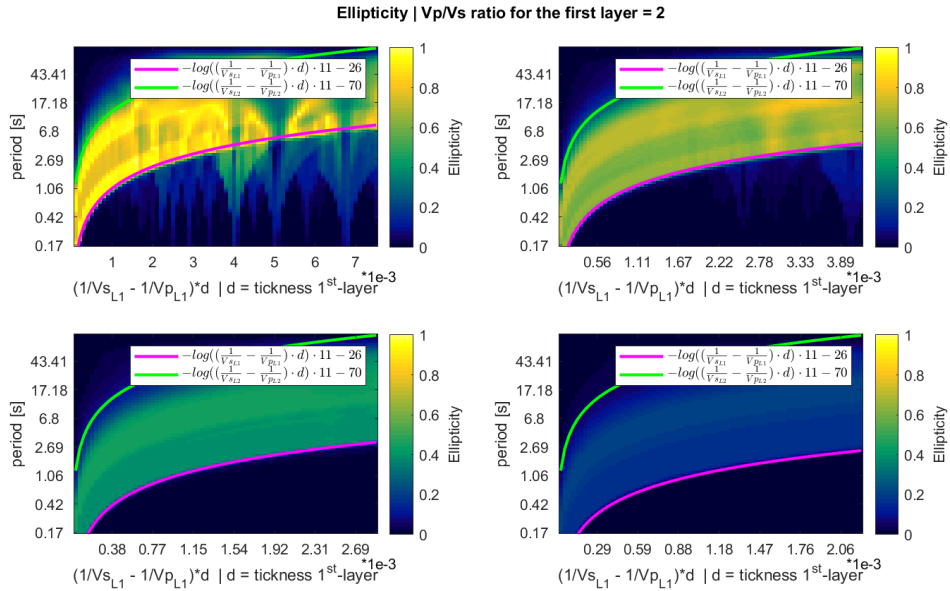
Figure A-1: Ellipticity for the velocity model 2.

A-2-2   Angle Estimation
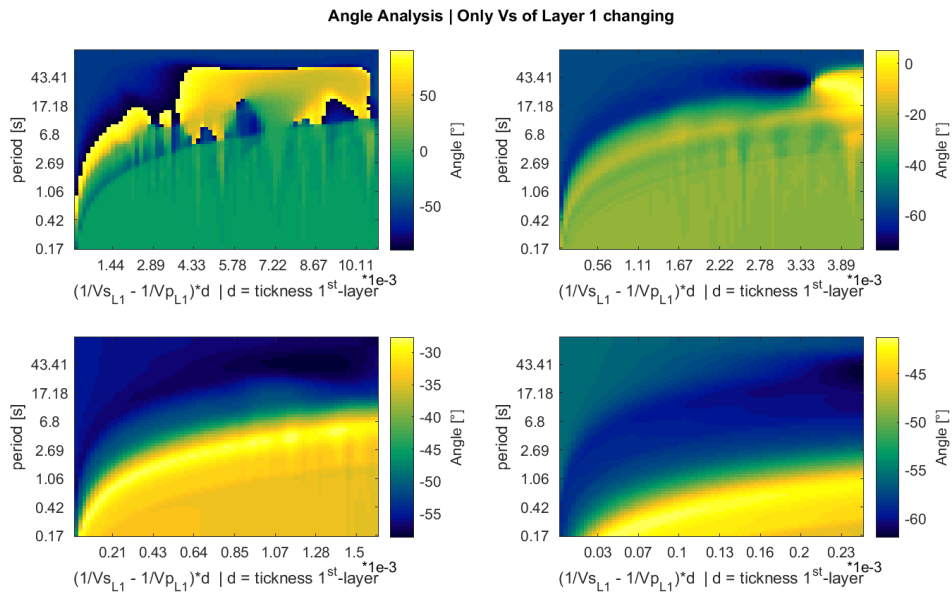
Figure A-2: Angle estimation for the velocity model 1.
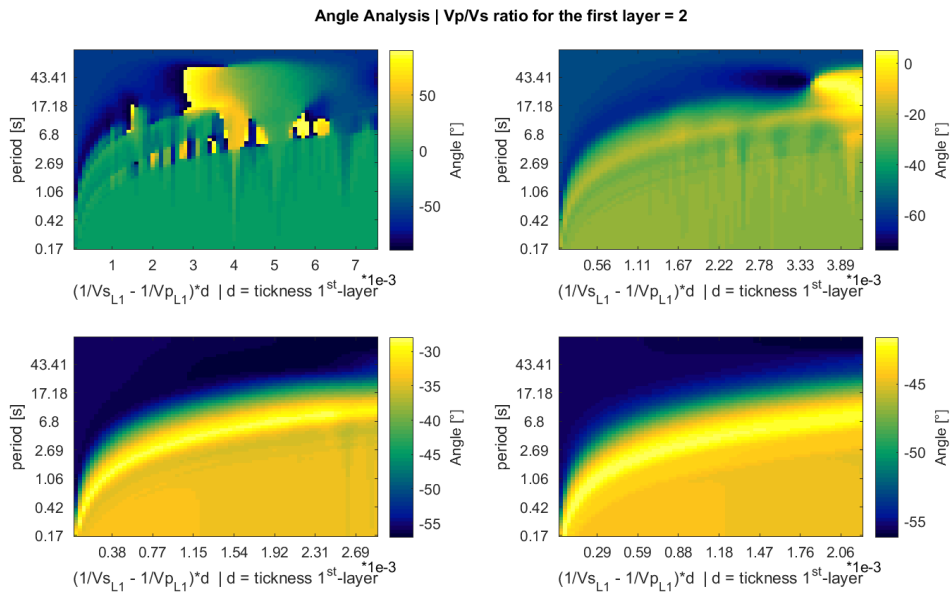
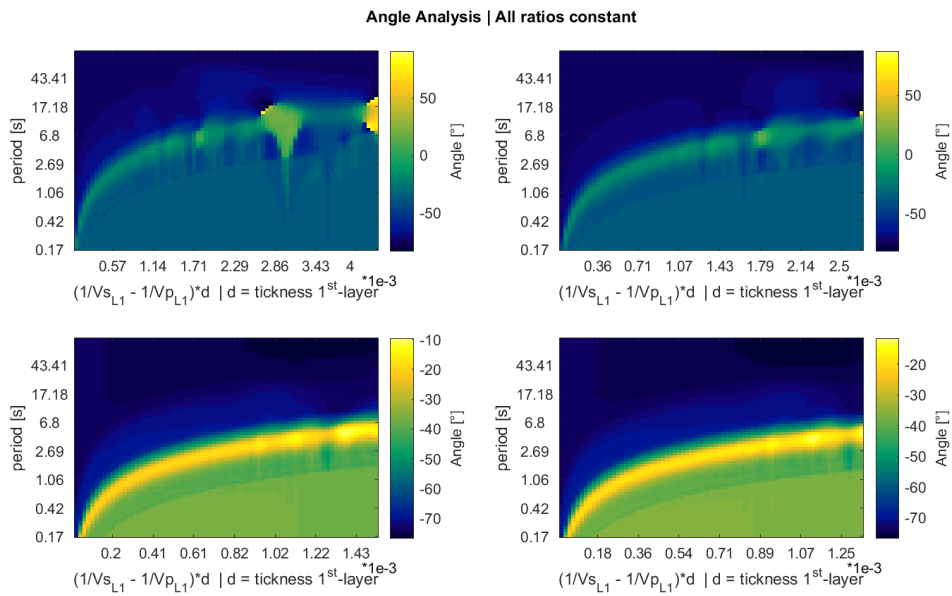**Figure A-3:** Angle estimation for the velocity model 2.

Figure A-4: Angle analysis for the velocity model 3. The angles for the regime 1 and 3 remain nearly constant. Regime 2 shows a non-gradual jump for the angle which leads to inaccurate velocity calculations in that part.

A-2-3   Cwt Velocity and Ellipticity Output
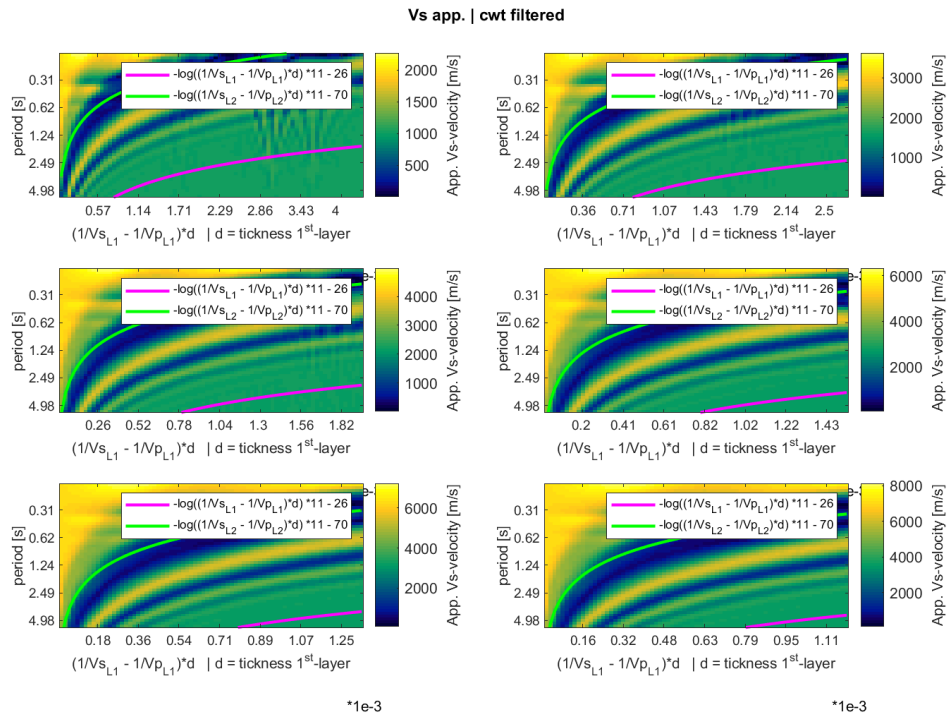
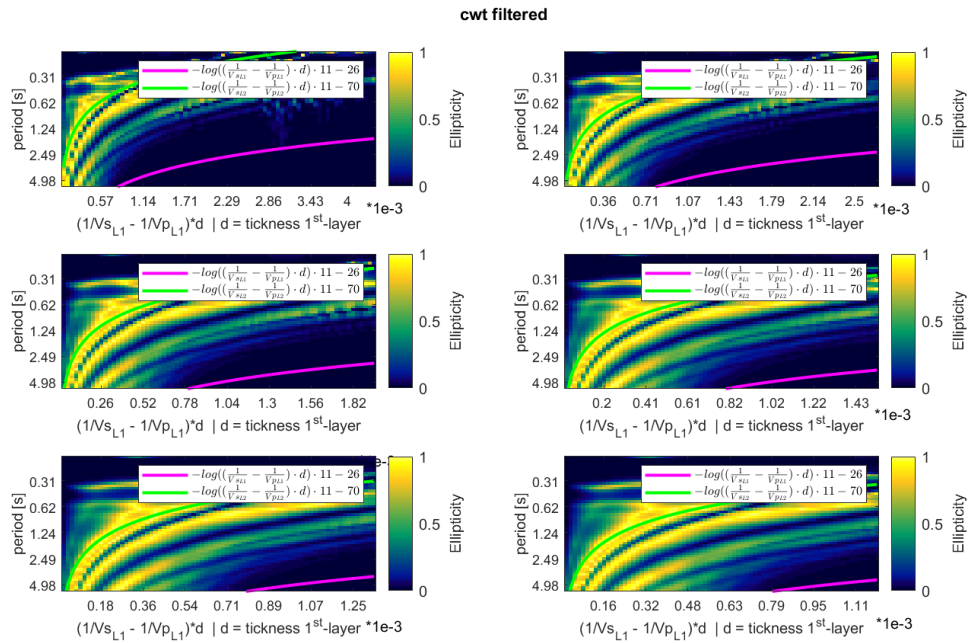**Figure A-5:** Velocity estimation with cwt 1-D wavelet transform with velocity model 3.

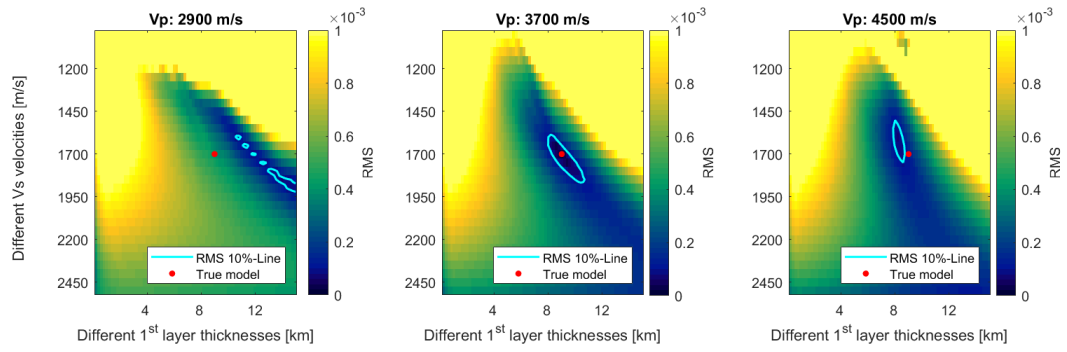**Figure A-6:** Ellipticity of cwt 1-D wavelet transform with velocity model 3.

A-2-4   Misfit RMS

Figure A-7: RMS misfit of the time between the P- and the PS-arrival.

Martian data

B-1 Results

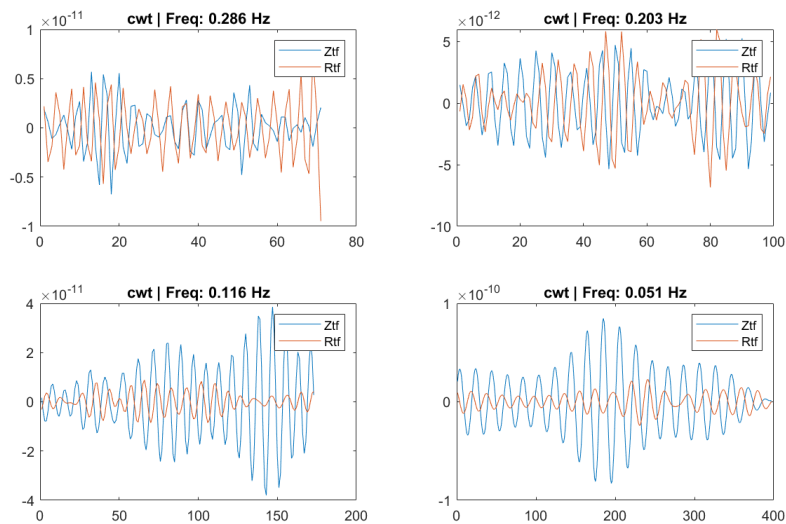### B-1-1 Cwt of the Event S0235b

Figure B-1: Horizontal and vertical component traces filtered at different frequency bands for the Mars event S0235b: 26. June 2019 (InSight Mars Data Service, 2022).